

Ionization Laser Optics Design for the Generation of Plasma

By

James Good

A Thesis Submitted for

Master of Science

In Optics & Photonics

at

Karlsruhe Institute of Technology

December 2013

Contents

1	Introduction.....	1
2	Topographical Overview.....	6
2.1	Direction Ionization.....	6
2.2	Field Ionization.....	7
3	Topographies Examined in Detail.....	9
3.1	Beamfolder.....	9
3.2	Multipass.....	9
3.3	Pulsetrap.....	10
3.4	Bessel Beams.....	13
3.5	Conclusion.....	16
4	Energy Distributions in Computer Simulations of the Topographies.....	17
4.1	Zemax.....	17
4.2	Matlab.....	23
4.3	Alternative Simulation for Idealized Systems.....	29
5	System Design.....	32
5.1	Overview.....	32
5.2	Prisms.....	32
5.3	Polarization & Birefringence.....	40
5.4	Quarter Wave Plate.....	41
5.5	Beamsplitters Overview.....	42
5.5.1	Overview.....	42
5.5.2	MacNeille polarizer.....	43
5.5.3	Birefringent Polarizer.....	44
5.5.4	Conceptual Experiment.....	46
6	Further Experimental Proposals.....	47
6.1	Pockels Cell Research.....	47
6.2	Plasma Probe.....	47
7	Conclusion.....	51
8	Bibliography.....	52
9	Table of Figures.....	54
10	Footnotes.....	56

10.1	Table of Alkali Metals	56
10.2	Table of Excimer Lasers	56
10.3	Preliminary Calculation of Solid-State Laser Energy	56
10.4	Solving Prism Amplification Factor for θ	57
10.5	Jones Matrices	58
10.6	Fresnel Plots for Various Materials at 193 nm	59

Ich versichere

wahrheitsgemäß, die Arbeit selbstständig angefertigt, alle benutzten Hilfsmittel

vollständig und genau angegeben und alles kenntlich gemacht zu haben, was aus

KSOP Study and Examination Regulations_English translation 18

Arbeiten anderer unverändert oder mit Abänderungen entnommen wurde

James Good

1 Introduction

The **Photo Injector Test Facility** (PITZ) at **Deutsches Elektronen-Synchrotron** (DESY) in Zeuthen is a ~30 m linear accelerator that accelerates electron bunches up to ~30 MeV at a rate of 10 Hz. It was constructed to develop and test technology for linear colliders and **free electron lasers** (FELs). Novel techniques for particle beam acceleration are being investigated for accelerators as the limits of diminishing returns are being reached with the current superconducting technologies used in both linear and circular accelerators as well as the geometric limitations of circular colliders.

One potential candidate is plasma acceleration of electrons. The use of plasma permits very high electric field densities constrained within very small volumes (1); thus plasma acceleration is one avenue of research within PITZ.

The proposed methods of plasma generation are either direct photoionization or **barrier-suppressed ionization** (BSI), otherwise known as field ionization, of an alkali metal vapour with a suitably low ionization potential. The former is a relatively simple, and direct, process while the latter is a non-linear effect.

To this end, a 'plasma cell' is currently being constructed in the mechanical workshop at DESY. This involves confining a homogenous column of neutral alkali vapour, with helium gas as a buffer, in a heat-pipe oven (2). The vapour can then be photoionized with a short-pulse (ns) laser in the **vacuum ultraviolet** (VUV) range for direct ionization, or with a 1 TW ultrafast (fs) Ti:Sa laser at 800nm for the field ionization.

Naturally, the simplest route to generating plasma is to use of direct ionization. This is a linear process, and relatively simple to model and predict.

While all of the alkali metals are highly reactive, this reactivity increases with increasing period of the Periodic Table. Therefore, Lithium is a desirable candidate for its relative stability compared to that of the other alkali metals. However, this stability also results in a higher ionization threshold of 5.39 eV⁽¹⁾ (230 nm) and a higher melting point of 454 K (3). Conversely, while Rubidium is highly reactive, it is desirable for its lower ionization threshold of 4.18 eV (297 nm), and melting point of 313 K. More importantly, **laser induced fluorescence** (LIF) can be used with Rubidium as a vapour density measurement tool.

Both Lithium (2) and Rubidium are potential candidates as they have both been successfully used in previous experiments (4) and offer low ionization potentials. Lithium is the primary candidate for direct ionization owing to its relative stability and greater ionization potential, despite its higher ionization threshold. Rubidium is a secondary candidate, despite its high reactivity and expense, because of LIF.

⁽¹⁾ Footnote 9.1: Table of Alkali Metals

All of the alkalis have low ionization energies which range from a high of 5.39 eV for Lithium down to lowest ionization energy of the Periodic Table of Cesium at 3.89 eV. Since all of the alkalis are then potential candidates they must also be considered by atomic cross-section of their vapour beyond the ionization threshold.

Atomic cross-section is the likelihood, or 'probability', that an ionization event might occur. For Lithium this is on the order of one Megabarn for the spectrum beyond the ionization threshold. However, for the rest of the alkalis the atomic cross-section is typically one order of magnitude less (5). Therefore, despite its higher ionization threshold, Lithium is easier to ionize for a given vapour density and fixed wavelength.

For Lithium the atomic cross-section peaks at 1.86 Mbarn at 170 nm (6). The two nearest fundamental wavelength lasers in that range are F₂ and ArF excimer lasers at 157 nm and 193 nm respectively^{2}. As foraying deeper into the VUV would only make designing the system harder from an optical standpoint, increase safety concerns owing to the greater ionizing ability of the laser and the highly toxic Fluorine gas, and because the difference in atomic cross-section between the two wavelengths is only 0.04 Mb, the ArF laser at 193 nm is clearly the superior choice. The ArF laser is also advantaged due to the availability of systems with high pulse energy.

Of course a frequency converted solid state laser, such as Nd:YAG at the 5th harmonic (213 nm), is also a possibility; the atomic cross-section at 210 nm is only 1.69 Mb, but as frequency conversion is highly inefficient at 20% (7), and owing to further factors explained later, the minimum pulse energy becomes untenable at 1.5 J.pulse⁻¹ at the fundamental wavelength.^{3}

As the typical lifetime of plasma is on the order of a microsecond (2), and the operating frequency of the accelerator is only 10 Hz, there is little reason to use a laser with a high repetition rate - this would simply create short-lived plasma inbetween electron bunches. Therefore an ArF excimer laser is desirable for its high power (>1 W) in the VUV and low repetition rate.

While Rubidium offers preferable ionization thresholds and vapour-pressure temperatures, it also has a much smaller atomic cross-section of 50 kBarn; 36 times smaller than that of Lithium. This makes the ionization of Rubidium vapour, for a fixed number of atoms, much less likely compared to Lithium.

Whilst this could be compensated with an increased amount of atoms, and thereby increased pressure, this might result in disadvantages due to the greater pressure differentials at the Kapton vacuum windows and increased scatter potential of the electron beam as it passes through the cell.

^{2} Footnote 9.2: Table of Excimer Lasers

^{3} Footnote 9.3: Preliminary Calculation of Solid-State Laser Energy

The initial objective is to build a setup based on the one from SLAC as published by (Muggli et al.) (2) to use as a launch pad unto further experiments. To this end, much of the same parameters, design features, and goals are applicable here. Although the goal at DESY is to demonstrate the self-modulation of a long electron beam. A homogenous alkali metal vapour is to be ionized to produce “cold” electron plasma. As dictated by our own needs for a plasma density of 10^{15} cm^{-3} (8), and assuming a similar ionization percentage of approximately 10% as obtained by SLAC, this results in a first estimation for the vapour density of 10^{16} cm^{-3} .

Given that the absorption coefficient (α) of a substance is proportional to the atomic cross-section (σ) and the number of atoms per cubic unit (N_v) in that substance:

$$\alpha = \sigma \cdot N_v \quad (1.1)$$

One can calculate that for Lithium’s atomic cross-section of 1.8 MBarn (6) at 193 nm, the absorption coefficient shall be approximately 0.0018 cm^{-1} . This is roughly a factor smaller than that of common window glass (9) in the visible spectrum, indicating a very low absorption.

Unfortunately, by virtue of the spatial constraints of the PITZ beam line, the ionizing radiation must be situated laterally to the electron beamline instead of longitudinally

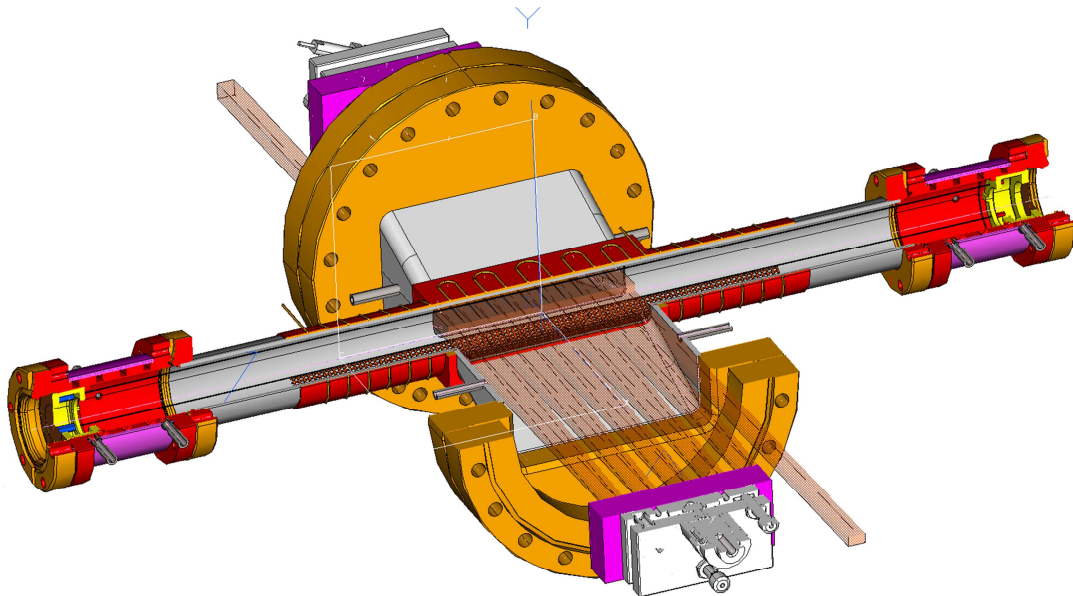


Figure 1.1: A conceptual overview of the prototype plasma cell and placeholder optics.

The process of ionization brings technological and engineering challenges:

- How to geometrically orientate the laser while maintaining a free path for the electron beam.
- How to focus, and confine, the 2.4 cm x 1 cm laser beam into a 6 cm-8 cm x 1 cm² vapour column.
- How to prevent lithium contamination of the optics. How to maximize the ionization process despite the low absorption coefficient (0.0018 cm⁻¹).
- How to achieve as-homogenous-as-possible plasma.
- How to do all of the above within the spatial confinements transverse to that of the electron beam and column.

The above considerations are heavily compounded by the issue that laser light with a wavelength of 193 nm is greatly attenuated, if not completely absorbed, by most common glasses, gases, crystals, etc. Insofar as it is known, there are a few, but limited, potential materials that can be used. The Silicon (SiO₂) glasses: Silica and quartz, the Fluoride glasses: Magnesium Fluoride (MgF₂), Barium Fluoride (BaF₂), Calcium Fluoride (CaF₂), etc. and some of the tetragonal birefringent crystals and their doped cousins: Ammonium dihydrogen phosphate (ADP), Potassium dihydrogen phosphate (KDP), deuterated Potassium dihydrogen phosphate (DKDP), Barium Borate (BBO), etc. (3)

The alternative method, field ionization, exploits the high electric field gradients provided by modern ultrafast lasers to suppress the ionization potential and permit the electron to tunnel through the potential barrier.

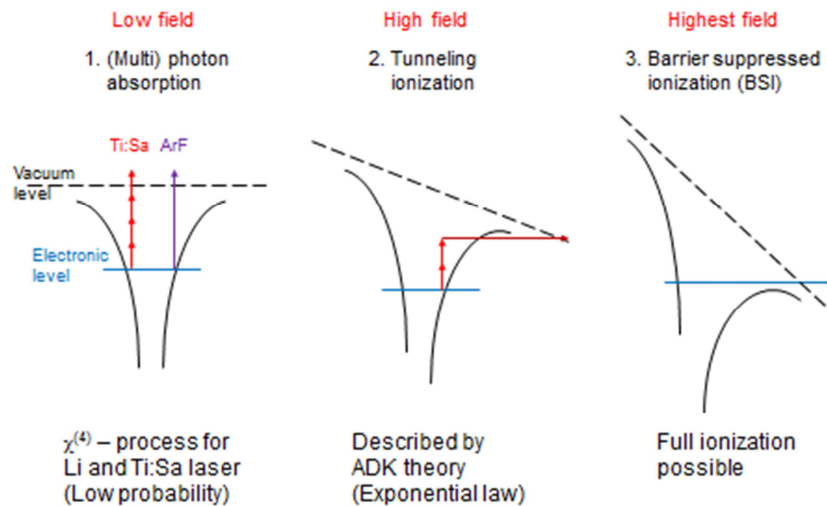


Figure 1.2: Field ionization potentials for different electric field gradients.

As calculated by (Tong et al.) (10), the threshold fluence required to do this is $5 \times 10^{12} \text{ J.cm}^{-2}$. This has the advantage of completely ionizing all vapour within any volume where this intensity is maintained. This requires a peak laser power in the TW range. This threshold

intensity is surely above the laser-induced damage threshold of essentially most, if not all, materials. Which in turn mandates that any optical setup must be carefully planned. The laser must also be in a vacuum so as not to ionize any atmosphere within its beampath.

Essentially the problem boils down to a beam shaping issue and a question of spatial orientation. If one desires on-axis [of the electron beam] ionization, then reflective optics may be used. While if one desires off-axis; lateral ionization, then a refractive solution may be more desirable. Two possible solutions might be an axicon coupled annular lens for line focus or an offset confocal resonator.

The goal of this work was to find practical solutions of the optical setups for ionizing an alkali vapour column in a plasma cell at PITZ for direct ionization with a UV laser and barrier threshold ionization with a Ti:Sapphire laser.

2 Topographical Overview

2.1 Direction Ionization

The first approach to model the direct photoionization is with the Beer-Lambert law:

$$E(z) = E_0 e^{-\alpha z} \quad (2.1.1)$$

It can be seen, owing to the very low minimum absorption coefficient of 0.0018 cm^{-1} , and assuming that all loss is as a result of photoionization, that very little ionization will occur. So, even if the beam were situated longitudinally with the vapour column, most of the energy would pass through the system as wasted energy.

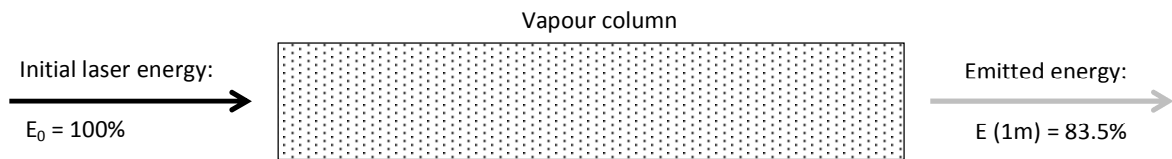


Figure 2.1.1: Conceptual overview of the nonlinear absorption of the Lambert-Beer law.

The immediately intuitive solution is to reflect the beam back into the system. This presents three potential topographies with three defining characteristics: active/passive, reflections per pass, and polarization-dependence.

<u>Beam-folding</u>	<u>Multi-pass</u>	<u>Pulsetrap</u>
Passive components	Passive components	Active or Passive components
>8 reflections/pass to cover whole volume	2 reflections/pass	1 reflection/pass
Polarization-Independent	Polarization-Independent	Polarization-Dependent

Table 2.1.1: Overview of possible topographies, and their features.

The first scheme, the beam-folder, is the most obvious solution. It is simple, cost-effective, relatively easy to align and requires no active components. Theoretically, N-amount of end mirrors could be inserted, approximating to a curved mirror, which would reflect the beam a near-infinite amount of times.

The multi-pass borrows its topography from laser-pumping schemes and its complexity and cost scale with the amount of mirror pairs. Again, given enough space, one could theoretically insert a near-infinite amount of mirror pairs for a large, but finite, amount of reflections.

The pulse-trap is unique in that it is dependent on the polarization of the beam and that it can employ an active or a passive **electro-optic** (E.O.) component. In a passive system the E.O. component is simply a quarter-wave plate, while in an active system it might be a Faraday cell or a switched Pockels cell.

For the pulsetrap the principle of operation is quite simple. The **polarizing beamsplitter** (Pol. B.S.) passes the polarized beam into the system which, on arrival at the E.O.-mirror pair, is flipped and reflected back again. Then the beam passes back through the system, whereupon the beamsplitter defines a new optical path for changed polarization; reflecting the beam back once more with the second mirror and trapping the laser pulse within in the plasma cell.

If the E.O. component is active it can be made to maintain the polarization and trap the pulse indefinitely (losses permitting). If the component is passive, the polarization is restored to the original polarization, reflected back through the system, and back upon its original optical path. Therefore, the amount of reflections can be either near-infinite, or four.

2.2 Field Ionization

For field ionization, owing to the high intensities required, it becomes desirable to concentrate the beam only within the intended ionization volume. An obvious solution is to use a Gaussian beam along the longitudinal axis of the beamline where the waist of the beam meets the minimum required width of the plasma column and the power along the beam is sufficient to ionize the minimum required length.

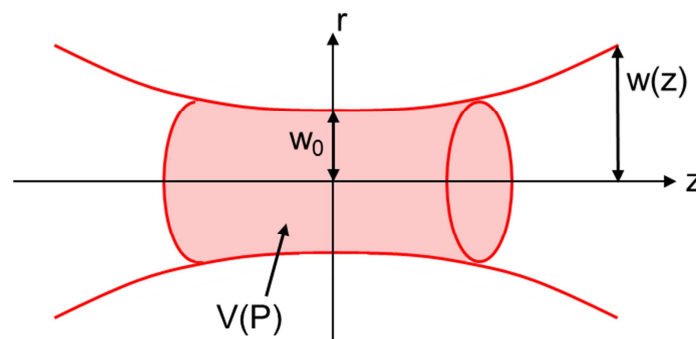


Figure 2.2.1: Gaussian beam overview.

Of course in order to couple the beam in, oblique annular mirrors must be fitted within the beamline. These mirrors would crop the ionizing beam effectively creating a “shadow” of unionized vapour directly along the path of the particle beam.

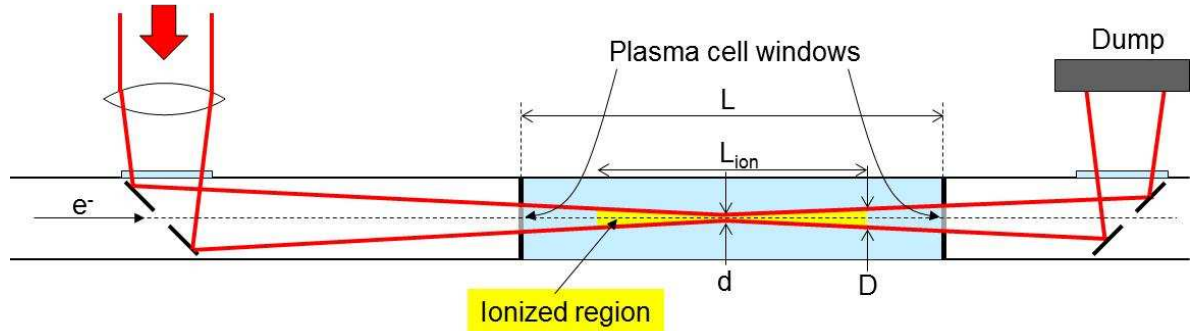


Figure 2.2.2: Focussing of Gaussian beam within plasma cell.

Alternatively, to avoid the “shadowing” of the particle beam, an axicon can be used to create a line focus at the annular mirrors, and a quasi-Bessel beam (11) at the region of ionization.

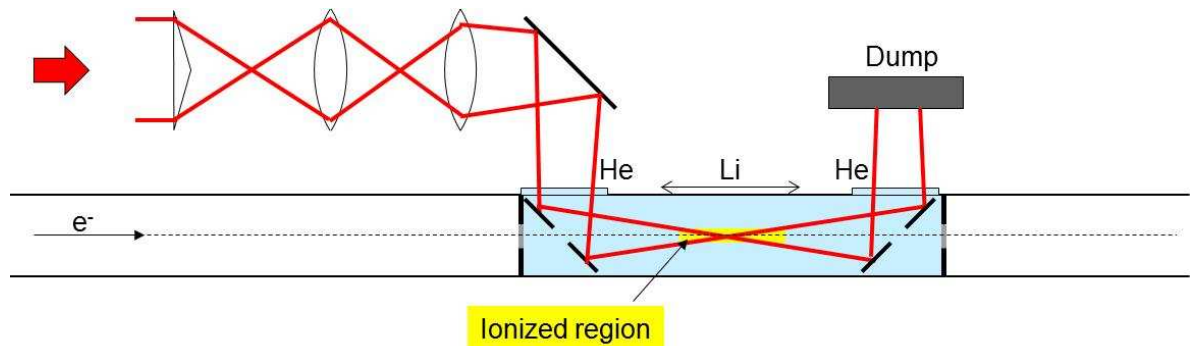


Figure 2.2.3: Bessel beam projected into plasma cell.

Ultimately, owing to practical constraints, field ionization is not a valid solution for the production of plasma at PITZ. As is shown later the physical limits of the beamline negate any optical topography and the cost of a suitably powerful laser (>300,000€) is prohibitive.

3 Topographies Examined in Detail

3.1 Beamfolder

With a beamfolder, one can place end mirrors (see Figure 3.1.1) to return the beam back through the volume. This might only be practically realisable for up to three reflectors, given the spatial constraints of the cell design. As the beam is folded upon itself this design also produces inhomogenities in the generated plasma. ‘Hotspots’ of plasma would be created by the mirrors where the beam is folded over upon itself and relatively cold spots where it diverges. Couple this with the concept of angled, exponentially decaying beam energies, and the conceived plasma inhomogeneity quickly becomes complex.

Compounding the difficulties is the fact that, even for the best ArF excimer mirrors at perfect **angle-of-incidence** (AOI), reflection is typically only about ~98%. Compared to a minimised pathlength of 16 cm between the plane mirror reflections, it is found that the minimum amount of energy deposited in the vapour (2.8%) is comparable to that deposited in the mirrors. As much energy is lost to the mirrors as to ionizing the vapour!

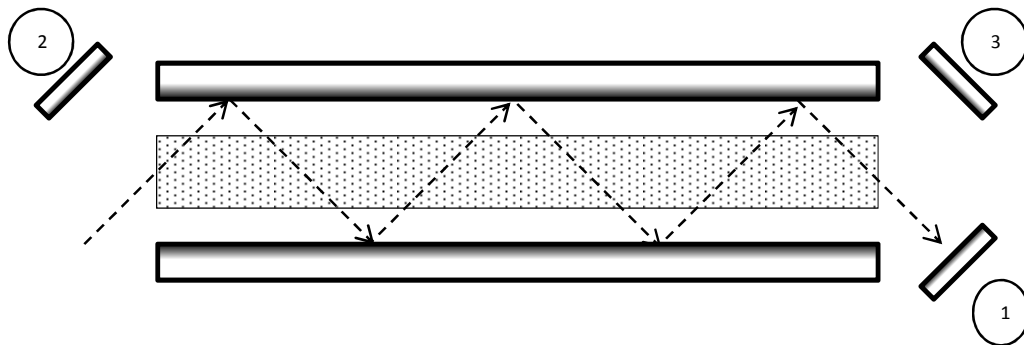


Figure 3.1.1: Schematic overview of a beam-folding topography. The plane mirrors are above and below the volume – the end mirrors are marked with 1, 2 and 3.

3.2 Multipass

With a multipass (Figure 3.2.1), the amount of passes through the system is limited only by the amount of mirror pairs one can space, align, and afford. Of course, this topography encounters very much the same problems as the beamfolder. While the amount of reflections required to pass the beam through the volume can be minimised to two-per-pass by beam expansion, the alignment versus spatial-requirements become increasingly difficult.

Pathlengths on the order of 1 m could be used to maintain shallow AOIs, but then atmospheric absorption potentially becomes an issue. Aligning a large beam with the central column, and within fractions of a degree, is also an issue. Such accuracy would also be compounded by thermal expansion and environmental vibrations.

With spatial constraints, short pathlengths could be used, coupled to large AOIs, but then the reflectivity of the mirrors quickly drops off by 15% over only three degrees deviation. Ghost reflections from the cell windows must also be contended with.



Figure 3.2.1: Overview of a seven-pass multipass topography.

3.3 Pulsetrap

The pulsetrap (Figure 3.3.1) offers even further reduced reflections-per-pass of one, combined with a potentially maximised reflection percentage of the mirrors and the simplest of alignments: straight. The only potential losses for the system are the beamsplitter and E.O. component.

For the vacuum ultraviolet there are two possibilities for the polarizing beamsplitter: an optically-contacted Magnesium Fluoride (MgF₂) Rochon prism with a nominal absorption of 12%, or a custom MacNeille thin-film polarizer with an estimated absorption of ~2-3%.

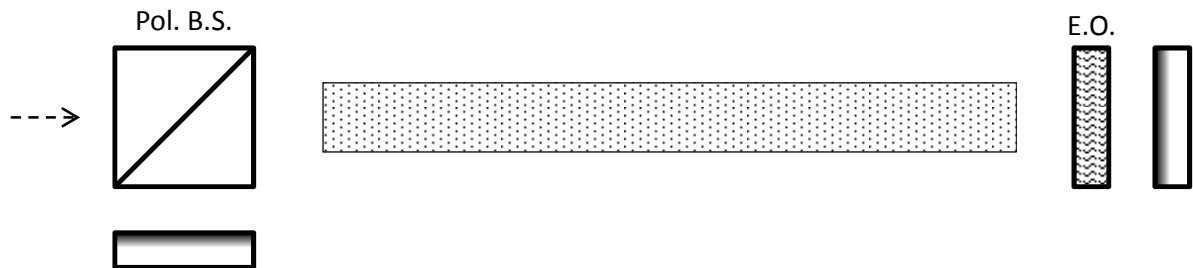


Figure 3.3.1: Conceptual overview of a pulsetrap.

For a passive pulsetrap utilising a quarter-wave plate, the losses and attenuation can be considered negligible as the waveplate needs be only as thick as an integer multiple of the wavelength.

For an active pulsetrap, it becomes a significant engineering challenge to find a suitable material for a Pockels cell or a novel new material (12) for a Faraday cell. Barium Borate (BBO), Ammonium Dihydrogen Phosphate (ADP), or Potassium Dihydrogen Phosphate (KDP) might be potential candidates for the Pockels cell, but attenuation is naturally a significant concern for all materials and very little research has been done in this area owing to the unusual working wavelength.

There are two manners in which to construct a Pockels cell: with the electric field situated longitudinally or transversely. The voltage required to rotate the polarization by a full half-wave is given by:

$$V_{\pi||} = \frac{\lambda}{2n_o^3 r_{63}}, V_{\pi\perp} = \frac{\lambda d}{2n_o^3 r_{22} L} \quad (3.3.1)$$

Where λ is wavelength, n_o is the ordinary refractive index at that wavelength, r_{ij} is the relevant electro-optic coefficient, d is the lateral distance between the electrodes, crystal width, and L is the pathlength of the crystal.

From the formulas it can be seen that for a longitudinal orientation the length of the crystal is limited only by the acceptable safety margin on the electrical breakdown of the local environment.

For lateral orientation the voltage is altered by the ratio of the lateral distance and the length.

Of course, for both orientations the laser induced damage threshold (LIDT) for the crystal must be kept in mind. As such a maximum fluence must be determined and therefore a minimum crystal width. This is complicated by electrode designs of the longitudinal orientation. If ‘transparent’ plane electrodes situated on the crystal ends are used then the LIDT determines the maximum fluence of the beam, however if ‘ring’ electrodes are used then the homogeneity of the field may be compromised for a sufficiently large crystal.

As previously mentioned, there are a few available electro-optic crystals available: BBO, KDP, ADP, DKDP, etc.

BBO has a large attenuation coefficient that is approximately 1.39 cm^{-1} at room temperature, but this is temperature-dependent and can be pushed down to 0.40 cm^{-1} (13). While ADP and KDP have coefficients one order smaller: ~ 0.13 and ~ 0.2 respectively (14).

The electro-optic coefficients of KDP, and DKDP, are temperature and wavelength dependent (15) (16); as wavelength and temperature decrease so too does the half-wave voltage. As ADP and KDP are of the same family, it seems reasonable to believe the same might be true for ADP. The electro-optic coefficients are also wavelength dependent for BBO (17).

The figure of merit of an electro-optical material is a measure of how well it performs. This is defined as the ratio between the electro-optic coefficient, or the half-wave voltage, and the absorption coefficient; V/α or r_{ij}/α .

Material	Electro-optic coefficient [pm.V-1]	Absorption coefficient (α) [cm-1]	Figure of Merit (FM) [10-14 m.V-1]
----------	------------------------------------	--	------------------------------------

BBO	r_{22} : 2.41 (633 nm)	1.39 – 0.40	1.73 – 6.03
ADP	r_{63} : 8.7 (633 nm)	0.13	66.9
KDP	r_{63} : 10.22 (550 nm)	0.2	51.1
DKDP	r_{63} : 25.8 (633 nm)	0.1	258

Table 3.3.1: Table of properties of electro-optic materials.

Assuming the values in Table 3.3.1 for 193 nm, a crystal width of 1 cm, an ordinary index of 1.5, and a pathlength of 0.1 cm the following half-wave voltages are obtained:

Material	n_o (266 nm)	Half-wave Voltage [kV]	Transmission (1 mm) [%]
BBO	1.757	73.82	96.08
ADP	1.580	2.81	98.70
KDP	1.560	2.49	98.02
DKDP	1.554	1.0	99%

Table 3.3.2: Table of Pockels cell parameters.

From these preliminary results it is unsurprising to find that DKDP is the best candidate. Though it is not unreasonable to believe the half-wave voltage would be in actual fact be lower with a reduced wavelength of 193 nm, and with cryo-cooling to improve the coefficients.

3.4 Bessel Beams

An axicon is an optical component which can be used to form a Bessel beam (Figure 3.4.1). Bessel beams are unique in that they are non-diffracting and form a line focus. Such a focus is ideal for the axial transmission of the beam through the particle accelerator for achieving the high intensities required for field ionization.

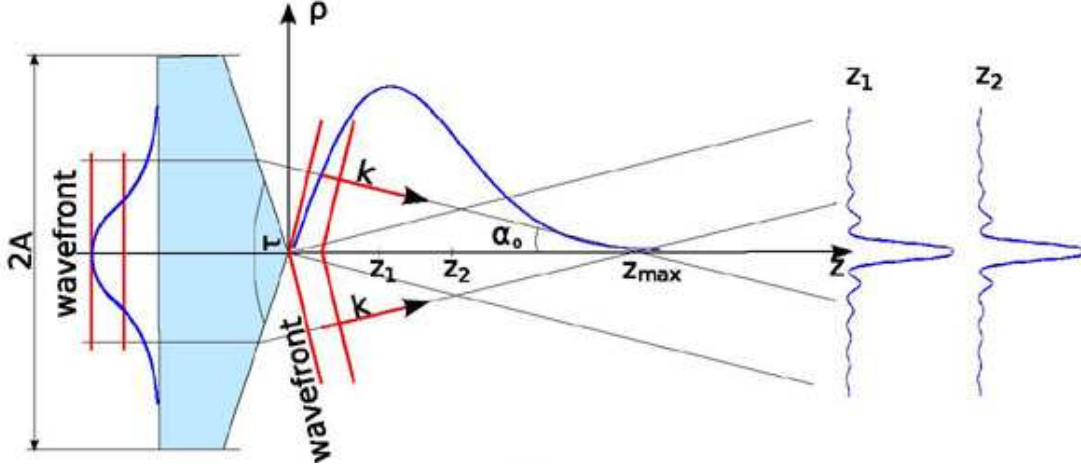


Figure 3.4.1: Bessel beam formation by a perfect axicon from a Gaussian beam. (11)

The optical intensity distribution of a Gaussian-Bessel beam is given by (11):

$$I(p, z) = \frac{4Pk \sin a_0}{w_0} \frac{z}{z_{max}} J_0^2(kp \sin a_0) \exp\left(-\frac{2z^2}{z_{max}^2}\right) \quad (3.4.1)$$

Where a_0 is:

$$a_0 = \sin^{-1}\left(n \cos \frac{\tau}{2}\right) + \frac{\tau - \pi}{2} \quad (3.4.2)$$

From the intensity distribution it can be seen that the radial intensity of a Bessel beam is dominated only by the Bessel function:

$$J_0^2(kp \sin a_0) \quad (3.4.3)$$

Where J_0 is a zero-order Bessel function of the first kind as a function of radial distance ρ , k is the angular wavenumber, and τ is the apex angle of the axicon. It can be found that for a commercially available axicon of apex angle 179.98° with an assumed refractive index of 1.5 at 800 nm that the FWHM of the central lobe shall be about 3.3 mm.

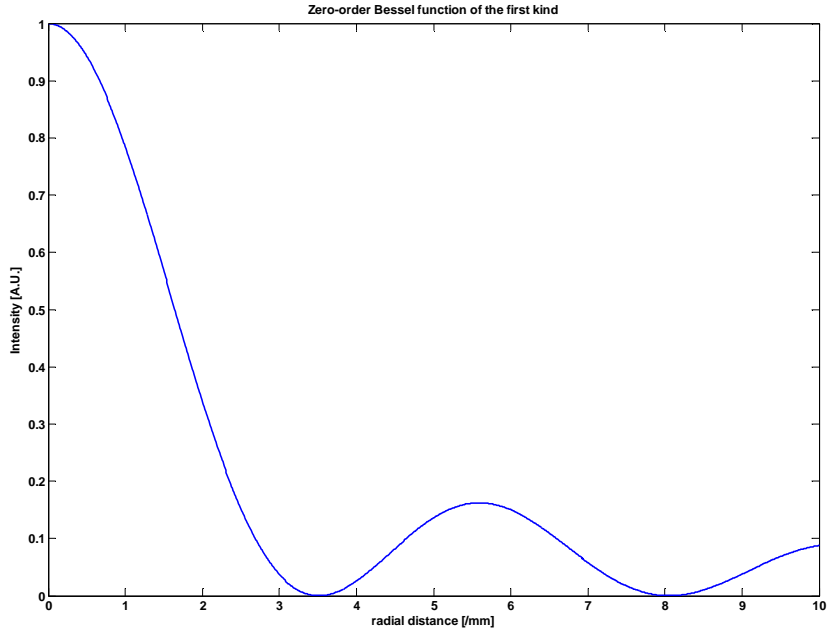


Figure 3.4.2: Radial intensity distribution for a Bessel beam with a FWHM of 3.3 mm.

Much like the relationship between focal length and depth of focus the maximum focal length (z_{max}) and the minimum of the first lobe of the Bessel beam (b_0) scale are related with apex angle of the axicon (τ):

$$z_{max} = r \frac{\cos a_0}{\sin a_0} \quad (3.4.4)$$

$$b_0 = \frac{2.4048}{k \sin a_0} \quad (3.4.5)$$

Where r is the waist of the incident beam and k is the angular wavenumber.

Mathematically the waist of the incident beam could be reduced by many factors to reduce the longitudinal length of the beam, but this is limited in reality; the rounding of the apex tip of the axicon which typically lies on the order of μm introduces modulation into the Bessel beam (11), and it is impractical to generate and align such microscopic Gaussian beams. The waist of the Bessel beam could also be modified by the angular frequency of the incident light, but this is limited by the practicality to visible light and the availability of the fs lasers required for field ionization.

For an incident beam of 780 nm on an axicon with a refractive index of 1.5 it can be seen that for the minimum required Bessel beam width of 1 mm the focal distance is ~ 18 m. Far too long a distance for the beamline in PITZ.

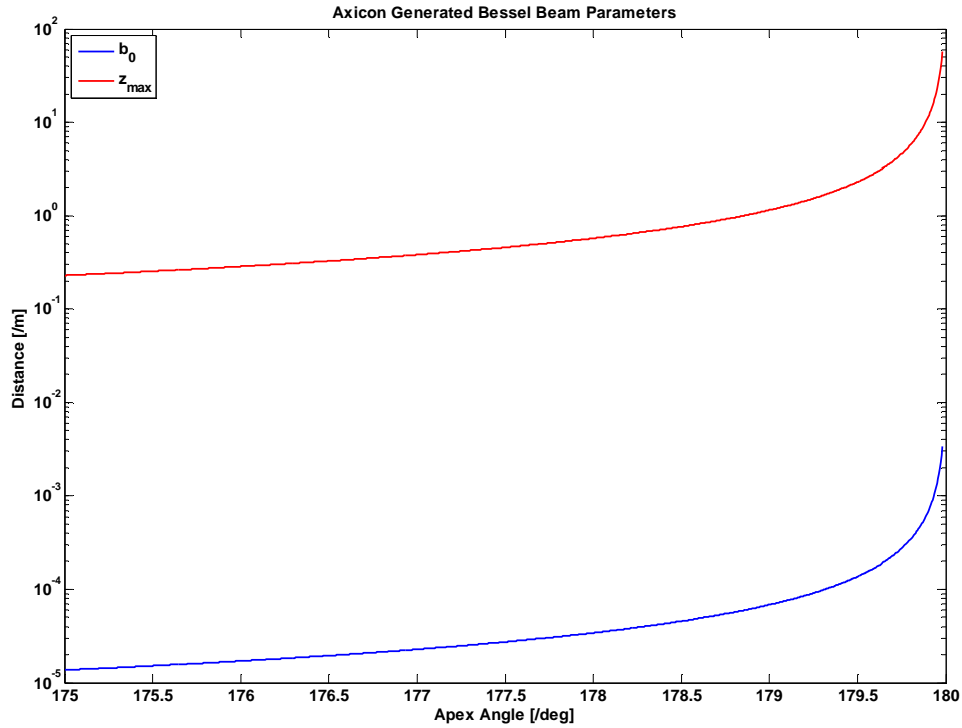


Figure 3.4.3: Lobe width (b_0) and focal distance (z_{max}) of an axicon-generated Bessel beam for an incident beam of 780 nm and a refractive index of 1.5.

It is proposed to modify the axicon by introducing a graded index (GRIN) along its lateral (18) or by annularly altering the local angle of incidence to produce a greater refraction further from the axis. Thereby geometrically maintaining the same focal depth but increasing the beam width. This would undoubtedly introduce perturbations into the Bessel beam and would have to be designed carefully from first principles to minimize this.

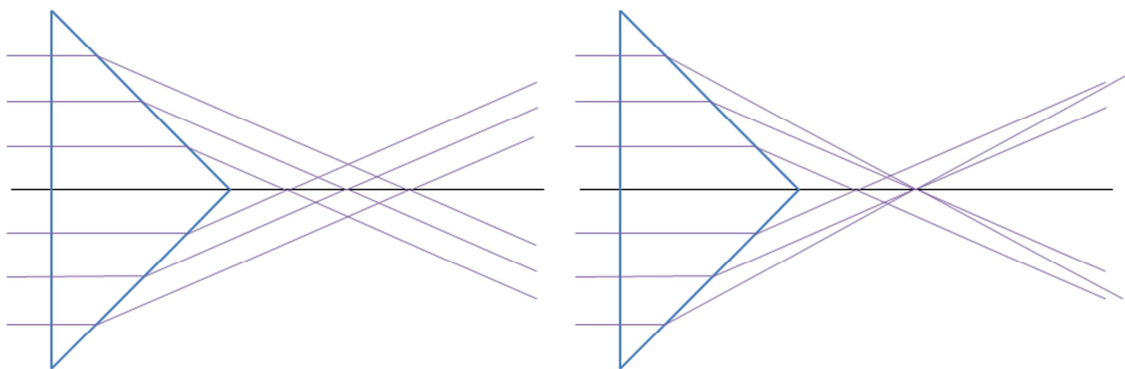


Figure 3.4.4: A typical axicon and a GRIN-modified axicon.

3.5 Conclusion

From the two possible ionization techniques available direction ionization was chosen – the pulsetrap topography. For direct ionization it is the most efficient topography, the simplest, and offers potential scalability with further improvements or requirements. Future developments in VUV Pockels cells, Faraday rotators, or material science could improve the efficiency of the optical components and enable an active pulsetrap topography.

These same practical and spatial considerations rule out field ionization; the beam length required for field ionization is far beyond what is available at PITZ coupled with the high cost of the required laser system. For larger LINACs with larger budgets such a technique might be more practical.

4 Energy Distributions in Computer Simulations of the Topographies

4.1 Zemax

Zemax provides a convenient first-approach with which to model the optical system. While Zemax was never designed for modelling gases undergoing ionization, it is possible to model the vapour as a fixed 'glass' with a specified attenuation coefficient, which is sufficient for a first-approximation basis.

Using the **Non-Sequential Component (NSC)** mode, the beamfolder can be simply modelled as a rectangular volume of Lithium "glass" confined between two reflective surfaces. The initial simulations were based on a geometrically idealized system with a 45° insertion angle for illustrative purposes.

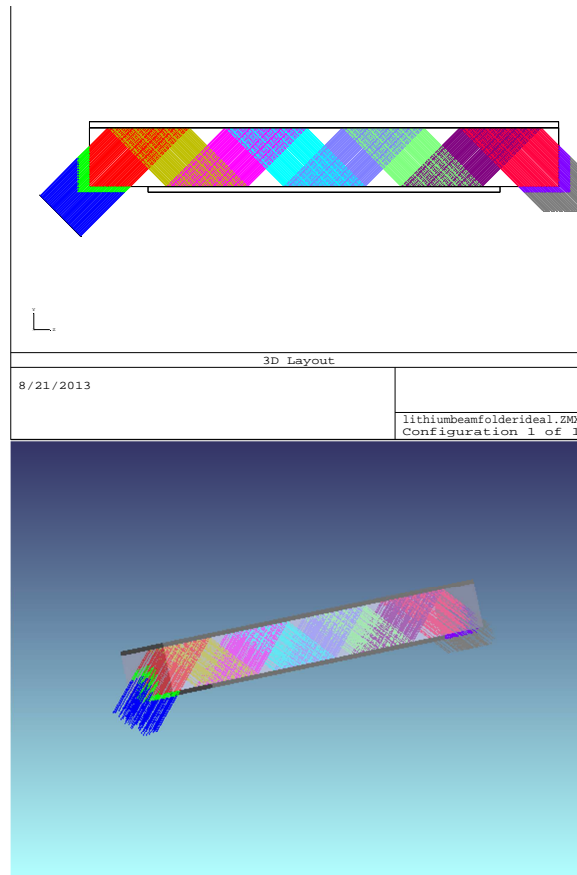


Figure 4.1.1: Geometrically idealized layout of the beamfolder used to illustrate the concept, simulated in Zemax.

One can clearly see that if the beam is not sufficiently broad for the geometry of the system that regions of high plasma density shall be created where the beam is folded over upon itself, regions of low plasma density shall be created in between, and plasma-free regions shall exist where the beam does not reach. Of course this is easily solved by a combination of beam expansion, mirror distance, and reflective angle.

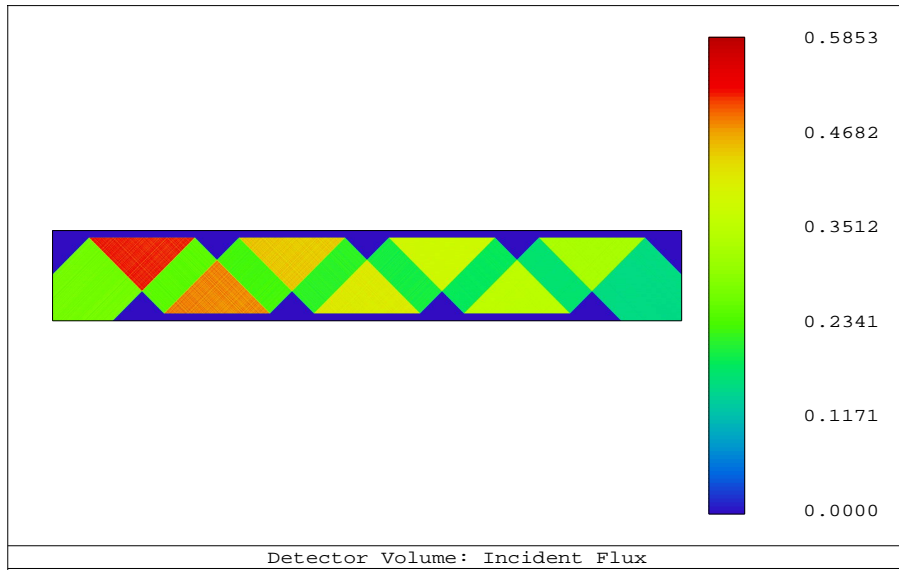


Figure 4.1.2: The absorbed flux in the detector volume of an idealized beamfolder with indicative 'hot' and 'cold' spots.

When this is expanded into the full situational parameters, the potential inhomogeneity of the plasma becomes apparent as an order of magnitude difference between one end of the cell and the other, even with "perfect" geometrical parameters.

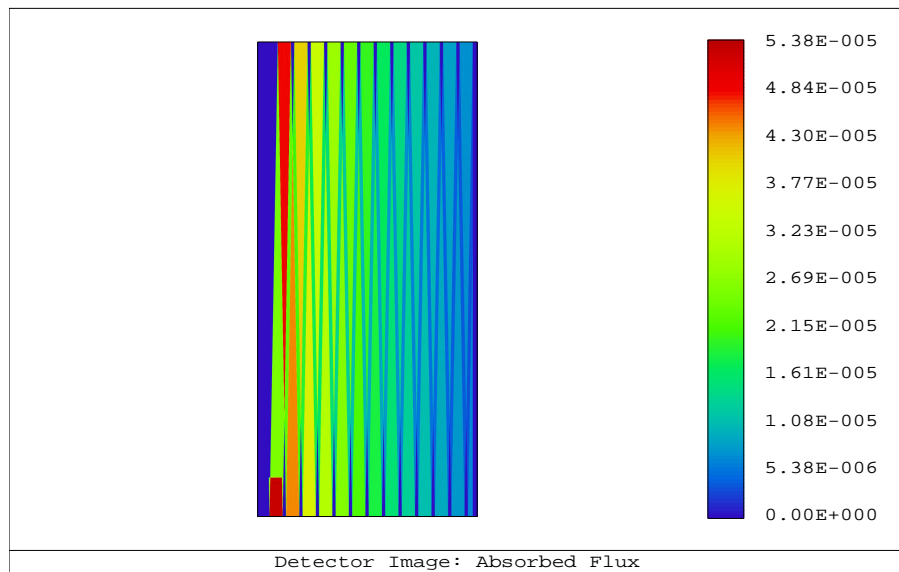


Figure 4.1.3: Fully modelled beamfolder with illustrative 'gaps' and an order of magnitude difference in absorbed flux.

In the diagram above one can once again see the gaps (left intentionally to illustrate), but also the (factor) difference owing to mirror losses and absorption in the Lithium. This clearly reveals the beamfolders to be a poor choice without corrective optics.

The multipass can be similarly modelled, in this case as a five-pass resonator with a beamdump, and detector volumes within the Lithium “glass”.

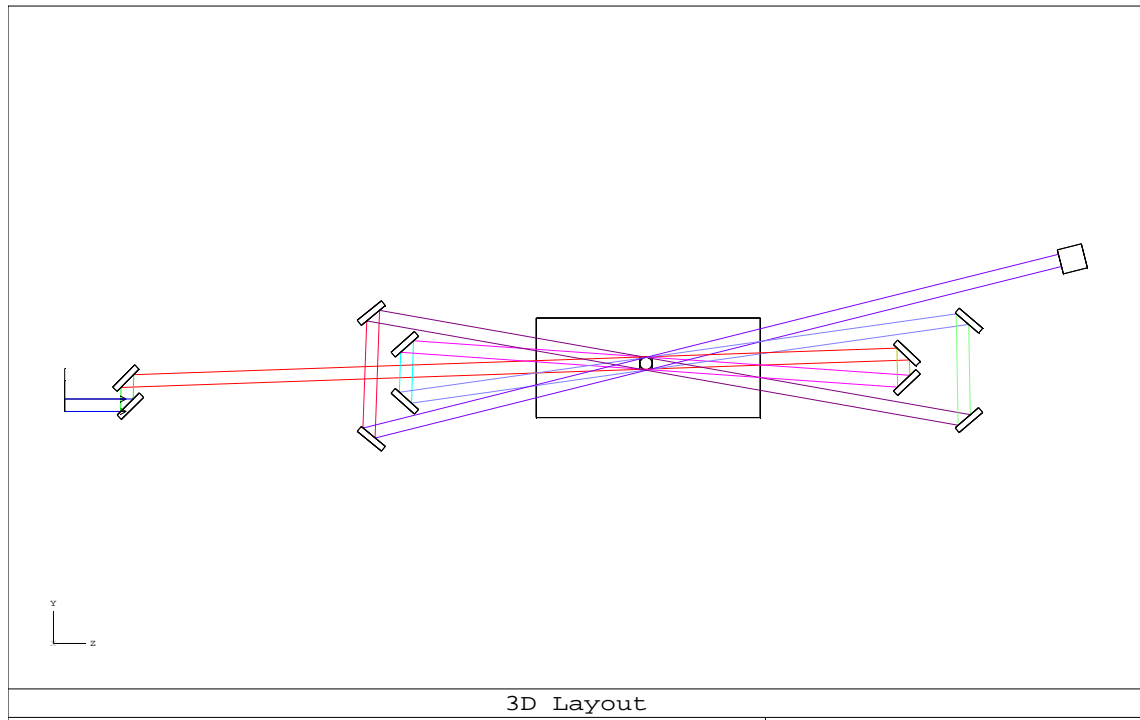


Figure 4.1.4: Schematic overview of a five-pass resonator in Zemax.

While imperfect, the simulation does give a ballpark figure for the potential amount of ionization in the central region. For example, for a 50mJ pulse incident on the system, approximately 5nJ shall be absorbed in each voxel of the 500x500x1 volume detector of 1 cm³ in a Lithium “glass” of density 10¹⁶ cm⁻³ ($\alpha = 0.018$). This can be summarized as 1.25 mJ absorbed within the cubic volume, and with each photon having an energy of about 10⁻¹⁸ J, this results in a quick estimation of the plasma density at 10¹⁵ cm⁻³.

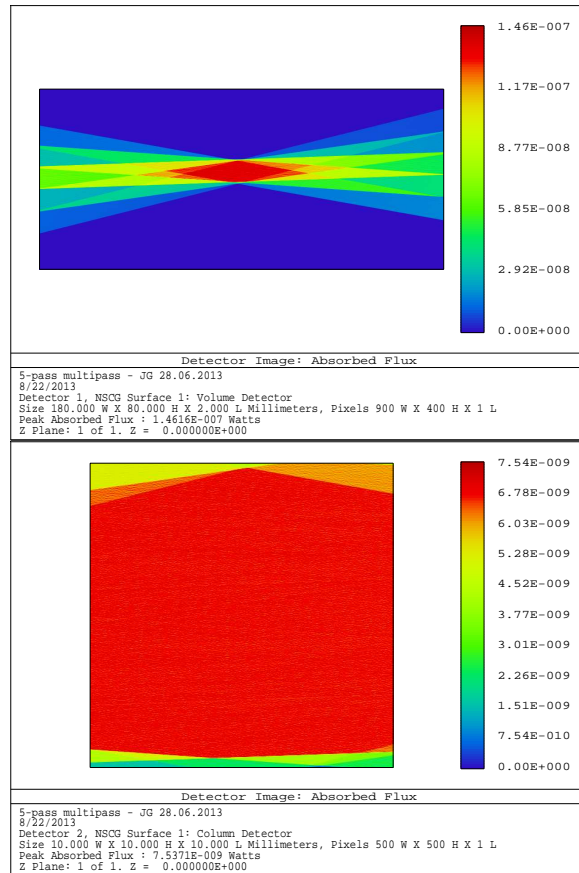


Figure 4.1.5: Fluxes through the Lithium volume for the five-pass multipass configuration.

While an active pulsetrap cannot be properly modelled in Zemax owing to the requirement of time-domain modelling, a passive pulsetrap can be approximately modelled with the suitable surfaces.

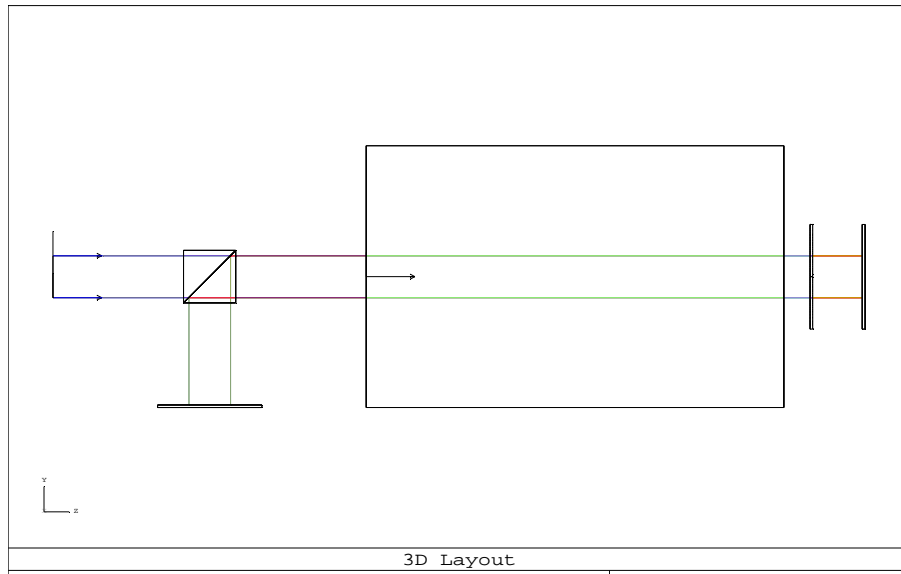


Figure 4.1.6: Conceptual simulation of a passive-pulsetrap in Zemax.

The sample 50:50 beamsplitter object supplied with Zemax is easily modified with the appropriate custom surfaces to model a polarizing beamsplitter, while the quarter-wave plate is tackled with a Jones Matrix surface. Everything else is easily handled with glass volumes, mirrors, and detectors.

This provides a first approximation for the plasma generation in a pulsetrap. For example, by moving the mirrors in and out of the system the energy exiting the system after one, two, or four passes can be determined and, by extension, the energy absorbed by the various loss mechanisms in the system can be inferred. The generation of the plasma can also be tracked with a detector volume.

The first pass through would be expected to generate a gradient as per the Lambert-Beer law, while each successive pass would be expected to “even out” the gradient and increase the absorbed energy in each voxel.

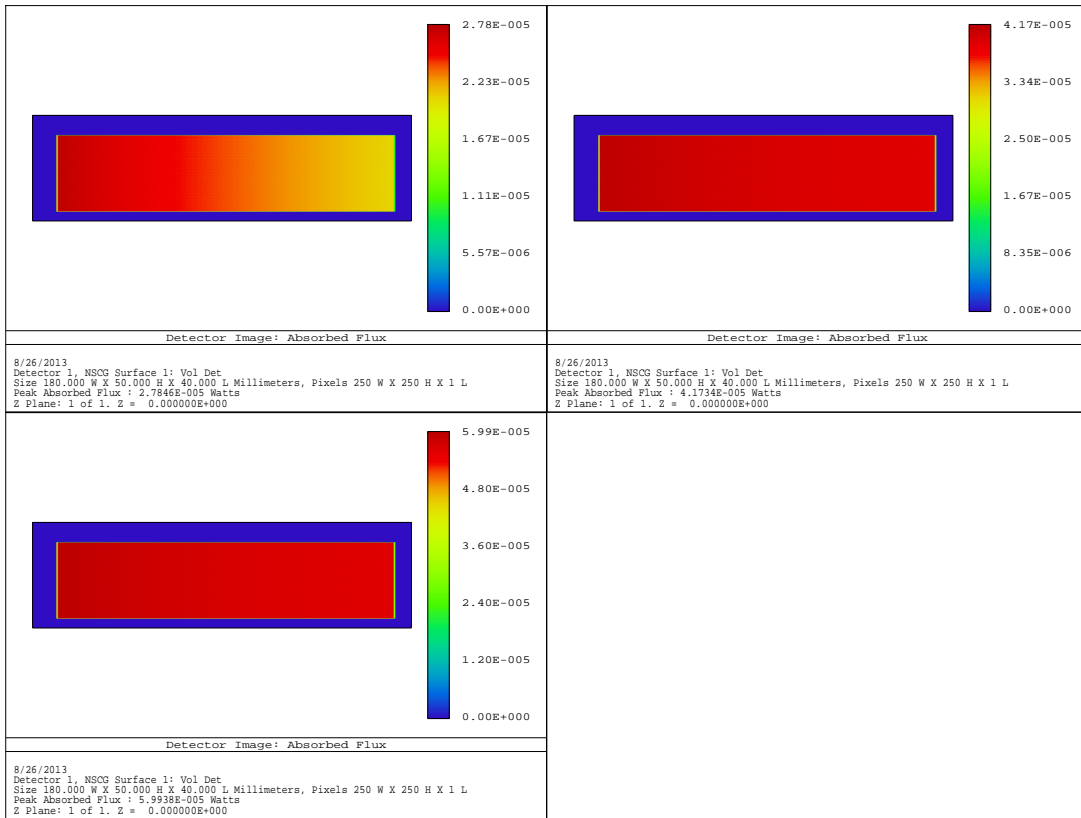


Figure 4.1.7: Zemax simulations of the passive pulsetrap.

While Zemax is a useful tool for the initial modeling of the potential topographies, it is limited in its scope and abilities. In order to define more accurate predictions the systems were mathematically modelled in Matlab to account for the different variables and features. This was only done for the multipass and pulsetrap configurations, as it was reasoned that the predicted losses in the beam-folder precluded the value in the complexity of modeling it.

Consequently it seems pertinent to continue to use Zemax as a physical model of the system, while using Matlab as a mathematical model.

4.2 Matlab

Assuming a simplified, linear system where a laser is passed through a volume of homogenously dense, pure vapour of some material and reflected back upon itself n -times.

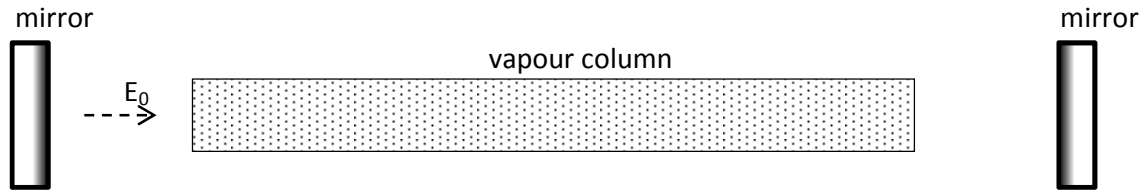


Figure 4.2.1: Overview of the simplified, linear system modelled in Matlab.

For the sake of convenience the initial laser pulse is placed within the system, propagating along the z -axis in what is, essentially, a plane mirror resonator. The absorption in the laser through the neutral vapour is modelled by the Lambert-Beer law:

$$E(z) = E_0 e^{-\alpha z} \quad (4.2.1)$$

Where $\alpha = \sigma \cdot N_v$, the atomic cross-section (σ) and the number of atoms of the vapour per cubic unit (N_v).

The plasma density was calculated by splitting the vapour column into normalized voxels, and recording the energy difference, ΔE , from the beam entering and exiting each voxel for one pass through the system starting with the normalized Energy of $E = 1$:

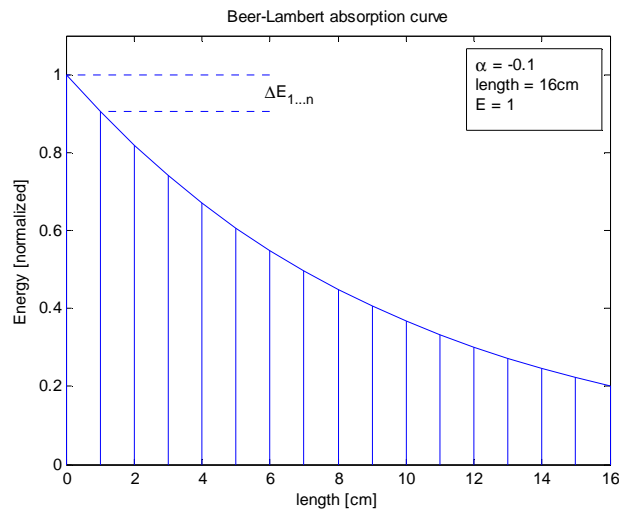


Figure 4.2.2: Example Beer-Lambert absorption curve quantized into voxels.

Assuming the absorbed energy is quantized into photons: $N_p = \frac{\Delta E \cdot \lambda}{h \cdot c}$, and every photon absorbed equates to an ionization event releasing one electron the resulting electron density (plasma), N_e for each voxel and the corresponding reduction of the vapour density is:

$$\Delta N_{v,n} = N_v - N_e \quad (4.2.2)$$

For any further n^{th} -pass the energy exiting the system is reinserted in the reverse direction, with any potentially applicable losses such as optical or environmental absorption and the ensuing plasma density is computed using the Beer-Lambert law on a voxel-by-voxel basis with the modified vapour density terms for each voxel. The energy entering each voxel equals the energy exiting the previous voxel.

The energy absorbed per voxel can then be summed and directly related that to the plasma density in each voxel for the number/amount of reflections through the system.

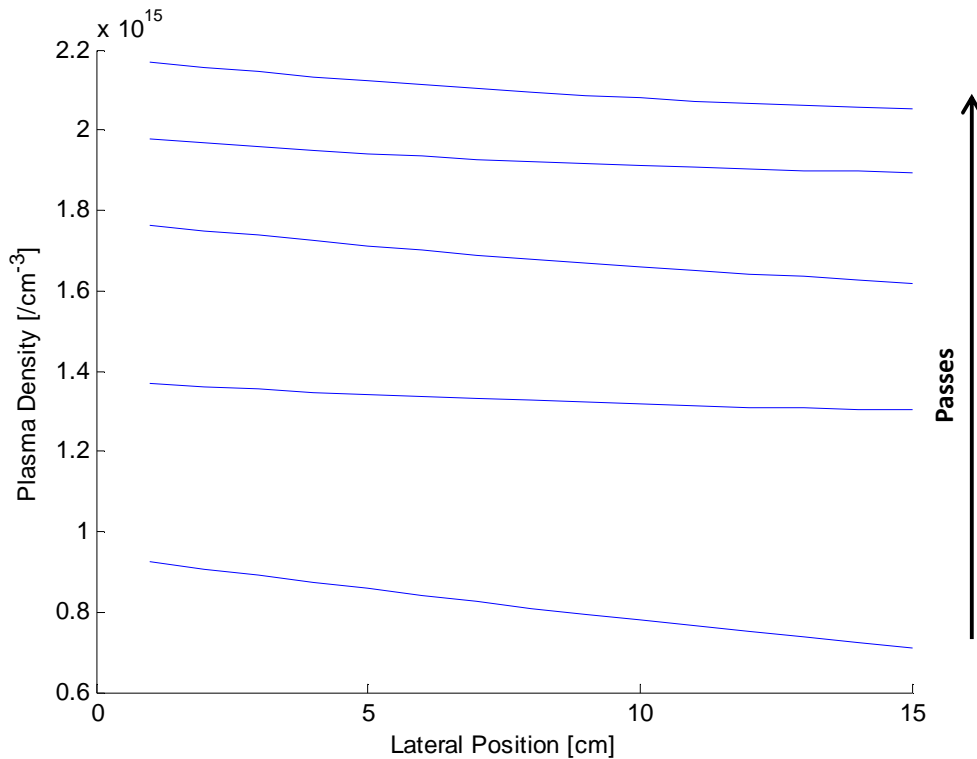


Figure 4.2.3: Lateral plasma density with each pass through an arbitrary system.

As can be imagined, every other pass partially compensates the exponential decay of the previous pass by overlaying a distorted, but mirrored exponential curve upon it. This indicates that an even number of passes should be preferred when possible.

As the system is symmetric along the longitudinal axis (the electron beam axis), if the beam is expanded longitudinally then the considered vapour volume may be 'sliced' and then only

one slice need be considered. This slice is then discretized into voxels as per the Matlab simulation above. This is demonstrated visually in the figure below.

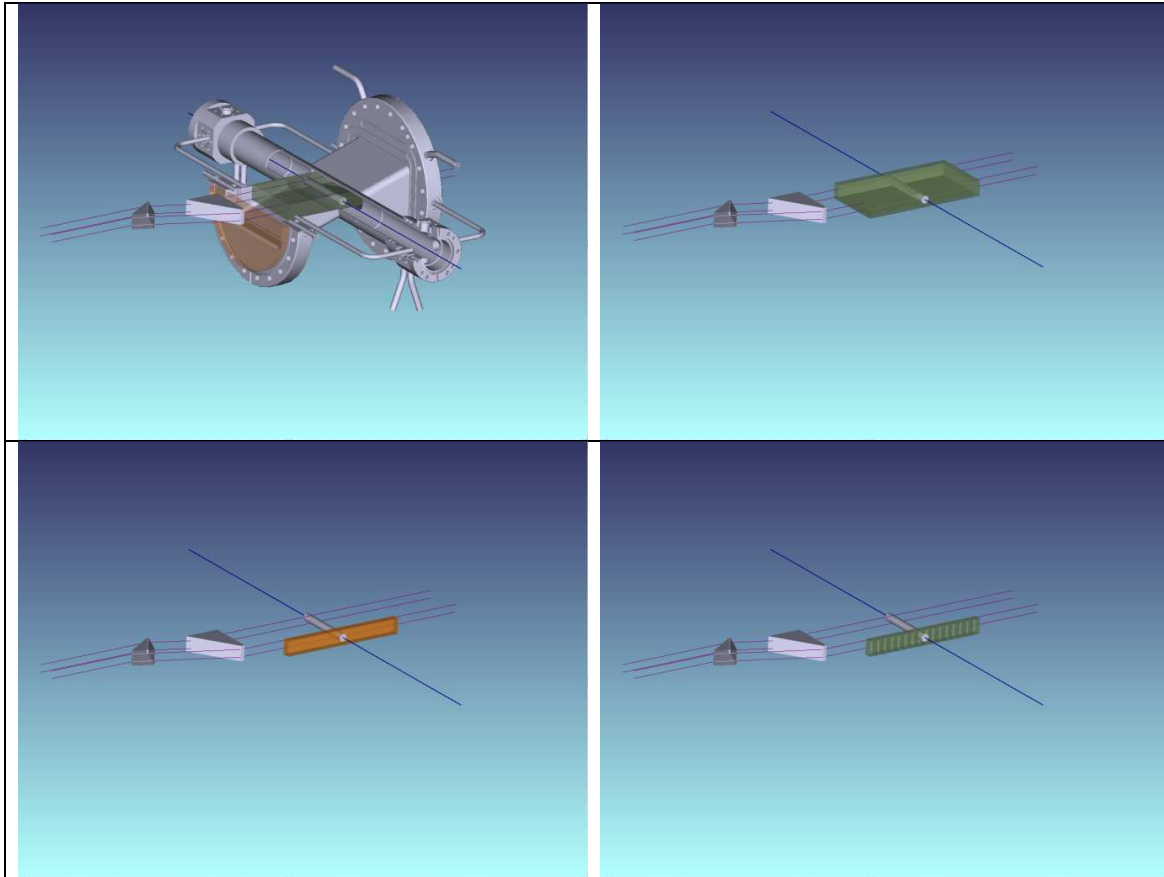


Figure 4.2.4: Visual representation of the 'slicing' and discretization of the vapour volume for simulation. (A) System overview. (B) The plasma chamber is removed. (C) The vapour volume "sliced". (D) The slice discretized.

In reality this results in expanding the laser beam one dimensionally from 2.4 cm x 1 cm to 8 cm x 1 cm, and as the beam is 400 mJ per pulse, this results in a fluence of 50 mJ.cm^{-2} over the area of the beam. Then only this 50 mJ need be considered one dimensionally as per the Lambert-Beer law.

Following this it is a relatively simple, albeit computationally laborious task, to recompute the plasma density for any specified voxel for any potential system configuration, i.e. system length, vapour density, total passes, system losses, etc. and plot the varying configurations as a surface. A useful plot in this case is the neutral vapour density – passes plot, as system length and losses can be fixed or determined.

There appears to be only a few potential loss mechanisms in a ‘cold’ plasma such as this. Rayleigh scattering and depolarization are possible, but given the short depolarization and scattering effects could be considered negligible.

For Thomson scattering, given such an extremely small cross-section, $\sigma_t = 0.665245$ Barn (19), and typically short path lengths and plasma density of any such experiment, the losses owing to Thompson (z.b. $\alpha_t \approx 10^{-9} \text{ cm}^{-1}$) are also negligible compared to any losses within the system optics ($\alpha_{\text{quartz}} = 0.01 \text{ cm}^{-1}$).

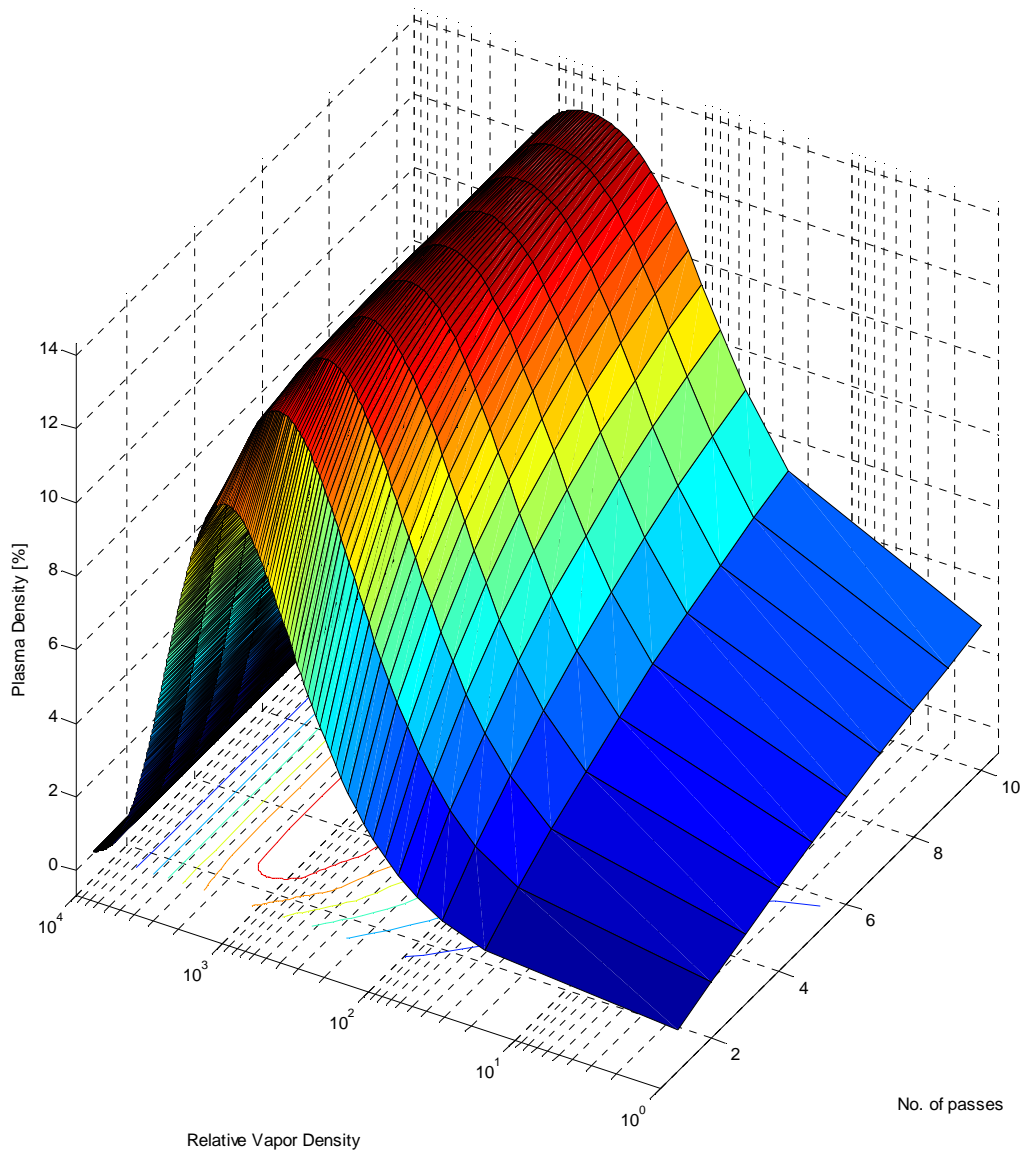
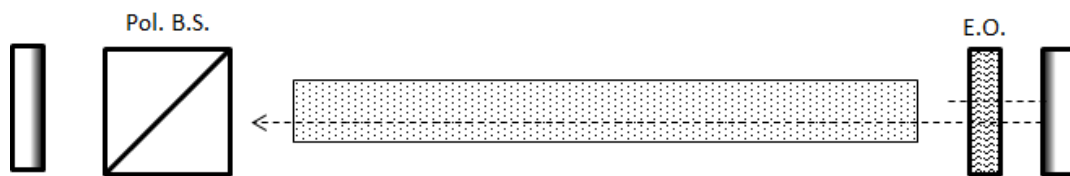


Figure 4.2.5: Plasma density surface map for a centrally located voxel in a Lithium vapour with an arbitrary laser energy, system length, and system losses.

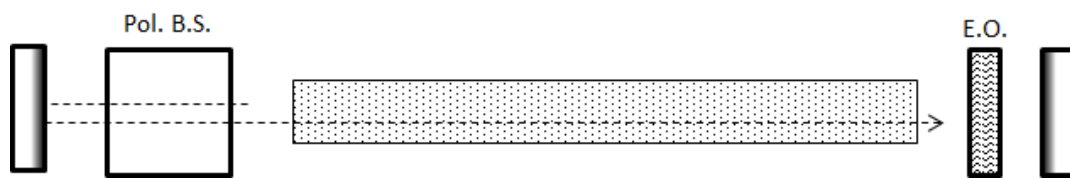
As can be imagined, the plasma density for a particular voxel increases with each pass of the laser beam, or with increasing vapour density as the absorption coefficient is proportional to the density of the vapour.

This eventually plateaus out with vapour density as the absorption becomes too great and the laser cannot penetrate the vapour to reach the selected voxel, or the with increasing passes the reduced laser energy and the depleted vapour population returns fewer and fewer ionization events.

This model is particularly ideal for the pulsetrap as the only modification required is to include the additional losses in the optics. For the initial pass, the losses can be considered as insertion losses, and for every subsequent Nth pass only the optics in the alternating paths need be considered.



For every even Nth pass only the losses in the end optics need be considered.



For every odd Nth pass only the losses in the junction need be considered.

Figure 4.2.6: Temporal overview of a pulsetrap.

The multipass configuration can be considered as a simplified version of this model as only the plasma density in the area of interest need be tracked and, as such, any other voxel may be treated as unionized vapour.

In conclusion, the topography can essentially be considered as an energy management problem. Or rather, how to minimize energy losses in a system where the desired process weakly absorbs energy. In this regard it soon becomes evident that owing to the unavailability of “perfect” mirrors in the VUV, fewer reflections are better. Conversely, it arises that shorter pathlengths are better; to conserve energy by minimizing the ionization of regions where it is unneeded.

It would be more energy efficient, and therefore preferable, to ionize only the column of interest in a longitudinal orientation, but this presents spatial and situational challenges of its own.

What can be concluded from the modelling is that for a given set of fixed system parameters (insertion losses, length, vapour pressure, etc.) fundamentally, the only differences between

the multi-pass and pulse trap are the practical limits of arrangement and the sources of losses in the systems.

	Practical Limit on Passes	Losses
Multipass	5	Non-minimized Mirror
Pulsetrap	4	Minimized Mirror + Potential back scattering

Table 4.1: Summary of two lateral ionization techniques.

4.3 Alternative Simulation for Idealized Systems

Ideally it would be preferred to introduce a chicane into the beam line to bend the particle beam in and out of the plasma channel. This is, however, impractical for very short distances (<1 m) and increasing beam energy as the engineering becomes increasingly challenging.

Consequently a chicane would only be used for long plasma channels or field ionization using axicons.

The length of the PITZ beamline is to be increased in the future and consequently it is possible that the plasma channel may be extended. As such the plasma density of a longitudinally ionized vapour channel with a cross-sectional area of 1 cm^2 and a length of 1 m was calculated. In an ideal case the chicane would be used to turn the electron beam around the mirrors and no annular optics would be required.

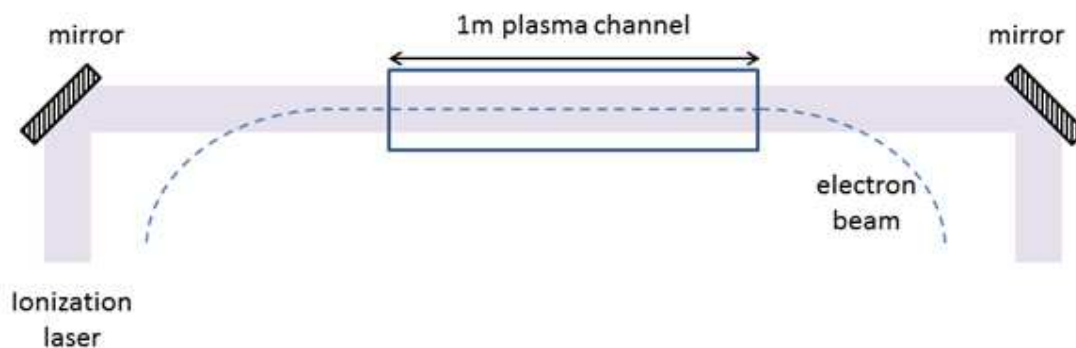
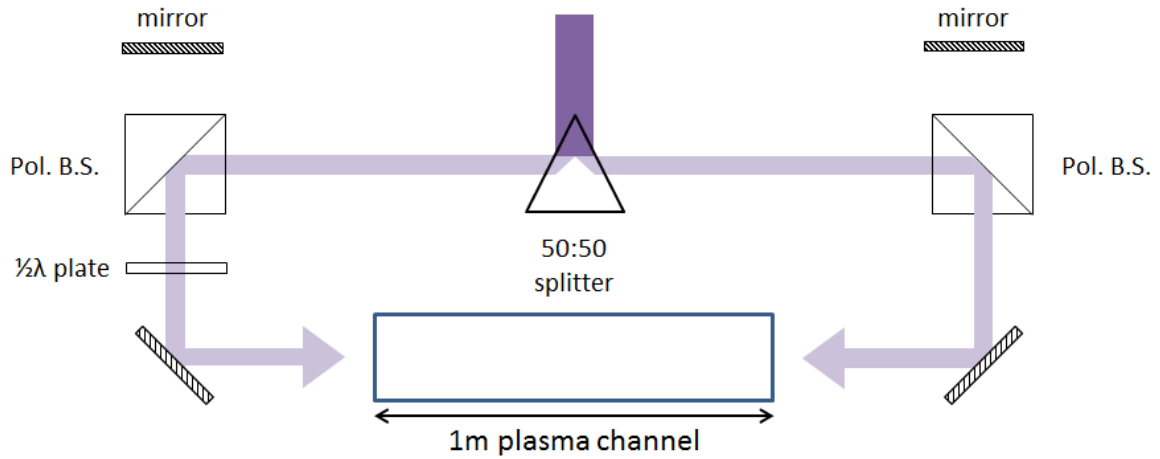
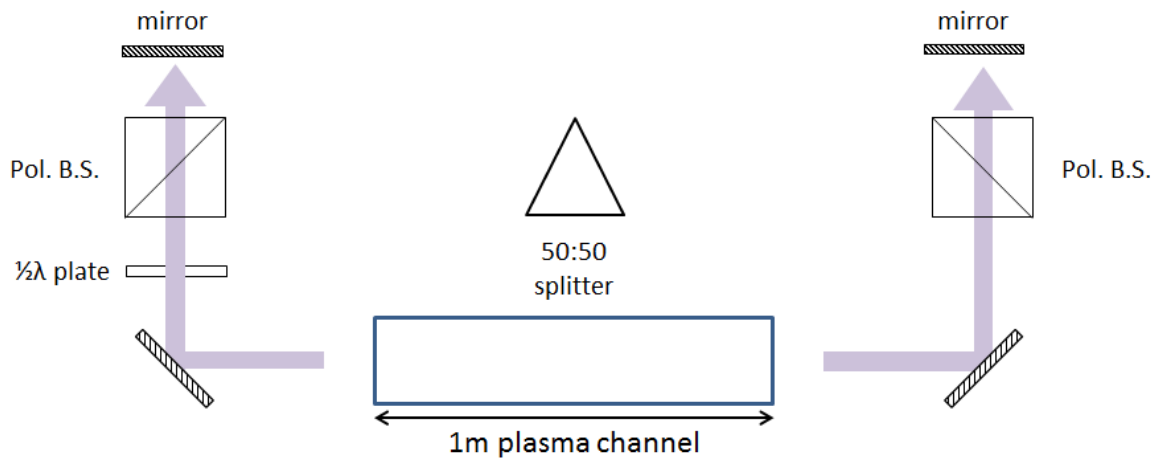


Figure 4.3.1: Idealized longitudinally ionizing plasma generation.

It should be quickly apparent that over such a long path the exponential absorption will create quite a large variance in the plasma along the length. Therefore it would be prudent to split the beam and combine it with a mirrored passive pulsetrap. (Figure 4.3.2)



Initial injection of the laser beam into the cell



Rotation of polarization and subsequent re-injection

Figure 4.3.2: Schematic overview of a symmetric pulsetrap for long, on-axis plasma generation.

In the above topography the pulse is split into two and the pulses are directed down arms of the pulse trap and laterally into the plasma chamber. The two pulses meet instantaneously in the center, overlapping one another and causing mirroring of the plasma at the center. The pulses having been rotated by the waveplate either prior or post- injection are then passed through the polarizing beamsplitters, and reflected back again into the plasma chamber further reducing the plasma variance.

For example, for a 400 mJ pulse split into two 200 mJ pulses longitudinally injected into the plasma chamber at a vapour density of 10^{16} cm^{-3} the plasma density distribution is as below Figure 4.3.3:

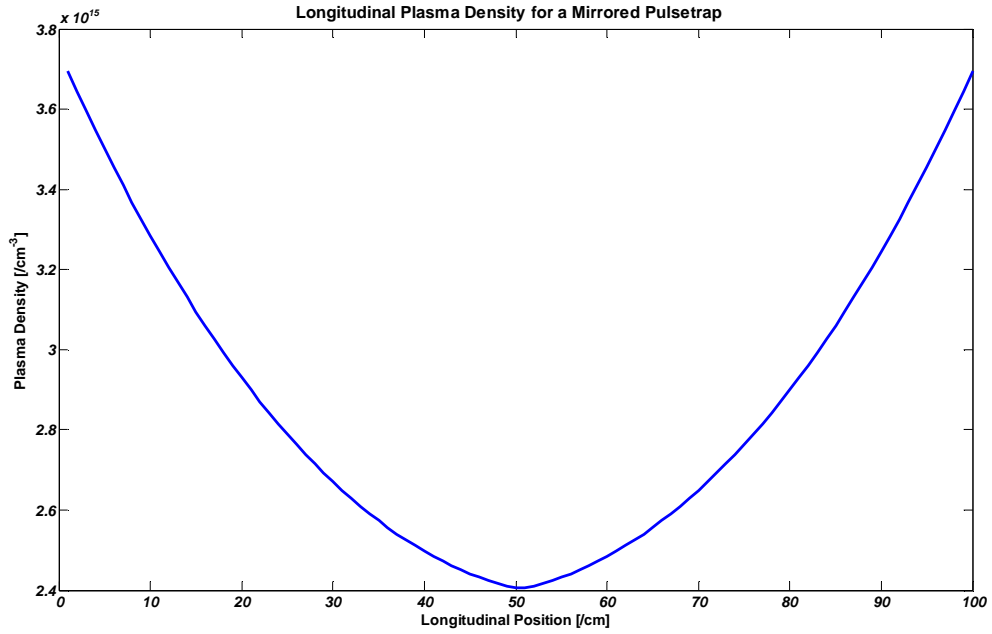


Figure 4.3.3: Plasma density for a longitudinally ionized two-pass passive pulsetrap.

While not completely homogenous the calculated plasma density varies by only $\sim 50\%$. Were a stronger laser pulse used it would be possible to completely ionize the ends of the plasma channel; saturating the plasma density and “pulling up” the central dip. For example, a 550 mJ pulse entering a vapour of density 10^{16} cm^{-3} would deposit $\sim 10 \text{ mJ}$ within the first cm^3 volume (as per previous calculations). Assuming a single photon equates to an ionization event this results in an ionization rate of $\sim 100\%$. This gives the threshold value for a laser pulse to begin to fully ionize the plasma channel at this vapour density.

System Design

4.4 Overview

The general concept of the topography is that of a “poor-man’s” optical isolator, wherein a quarter-wave plate is used in place of a traditional Faraday rotator or switched Pockels cell. A Faraday-based optical isolator is superior; it can handle non-linearly polarized light, is switchable, and not sensitive to the polarization angle.

Insofar as can it be ascertained, no such Faraday rotator exists for the vacuum ultraviolet. There have been novel materials developed recently (12), but they are currently unavailable commercially, or academically. Nor does it seem that a suitable Pockels cell exists with the required switching frequency or sufficient transmission. Intra-vacuum electrical arcing and dielectric breakdown are a concern with the design such devices.

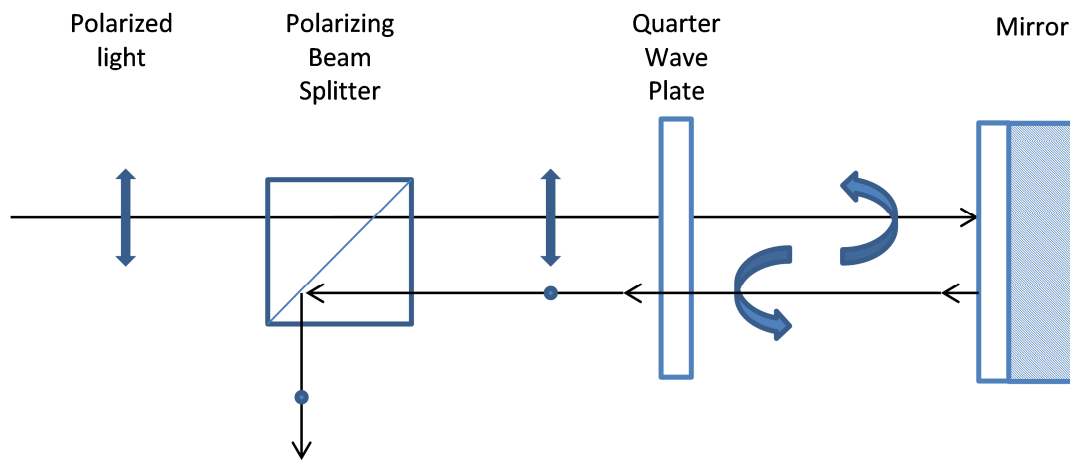


Figure 4.4.1: Conceptual schematic of a Poor-man’s optical isolator.

The isolator operates by the following principle: the quarter-wave plate is orientated at 45° with respect to the polarized light, which converts the linear polarization into circular polarization. The now circularly polarized light reflects off the mirror, flipping the handedness of the polarization. The now oppositely circularly polarized light once again passes through the wave plate and is converted into polarized light that is orthogonal with respect to the original beam. The whole operation can be summed up as a half-wave plate and a reversal of direction.

For reasons outlined previously, the eventual design selected was the passive pulsetrap as it had equitable plasma generation capabilities and cost compared to the multipass design but maintained a far simpler alignment process. In order to adapt the design to the actual system specifications a few modifications were required.

4.5 Prisms

The desired plasma column length is between 6 cm and 8 cm. Given that the laser system’s initial beam dimensions are 2.4 cm x 1 cm obviously the beam needs to be expanded in one dimension. To this end prisms were included in the design to expand the beam to the necessary dimensions and to compress it back down for retardation and reflection.

These prisms were custom-made for our purpose as, once again, the requirements lie outside standard optics catalogues. The design was fairly elementary; the beam expansion factor is easily given by the following derivation, assuming an ambient environment of vacuum/air:

$$d_2 = h \sin(90 - \theta_r) \quad (4.5.1)$$

$$d_2 = \frac{d_1}{\cos(\theta_i)} \sin(90 - \theta_r) \quad (4.5.2)$$

$$d_2 = \frac{d_1}{\cos(\theta_i)} \cos(\theta_r) \quad (4.5.3)$$

$$\frac{d_2}{d_1} = \frac{1}{\cos(\theta_i)} \cos\left(\text{asin}\left[\frac{\sin(\theta_i)}{n_2}\right]\right) \quad (4.5.4)$$

Defining the beam expansion factor as $\frac{d_2}{d_1} = F_x$ equation (4.5.4) can also be solved⁽⁴⁾ for θ_i :

$$2\theta_i = \text{acos}\left(2\left[\frac{n^2 - 1}{F_x^2 n^2 - 1}\right] - 1\right) \quad (4.5.5)$$

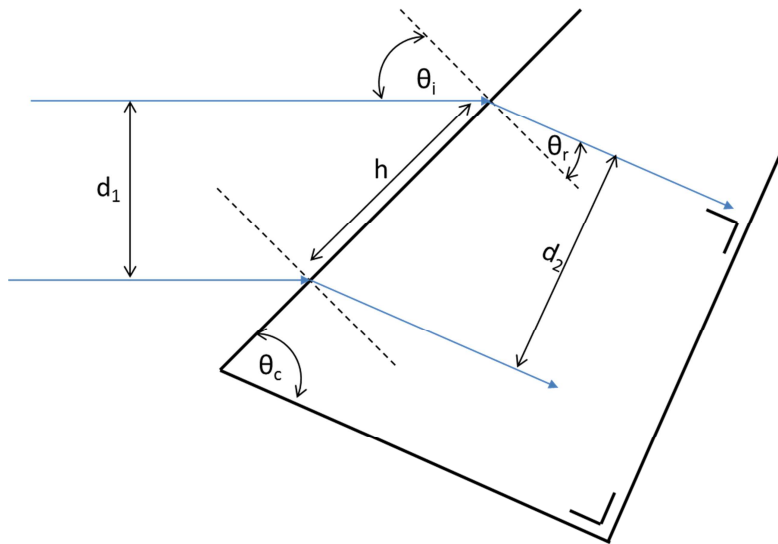


Figure 4.5.1: Schematic overview of a prism expander

For simplicity of design, it is assumed that the refracted beam shall be incident on the rear interface at normal incidence, therefore the cut of the prism, θ_c is given simply by:

$$\theta_c = 90 - \theta_r \quad (4.5.6)$$

$$\theta_c = 90 - \text{asin}\left[\frac{\sin(\theta_i)}{n_2}\right] \quad (4.5.7)$$

⁽⁴⁾ Footnote 9.4: Solving Prism Amplification Factor for θ

These necessary two values are easily calculated and plotted via a Matlab script for design purposes. Given a refractive index value of 1.42767 of Magnesium Fluoride (MgF₂) glass at a wavelength of 193 nm, the expansion factors are plotted as:

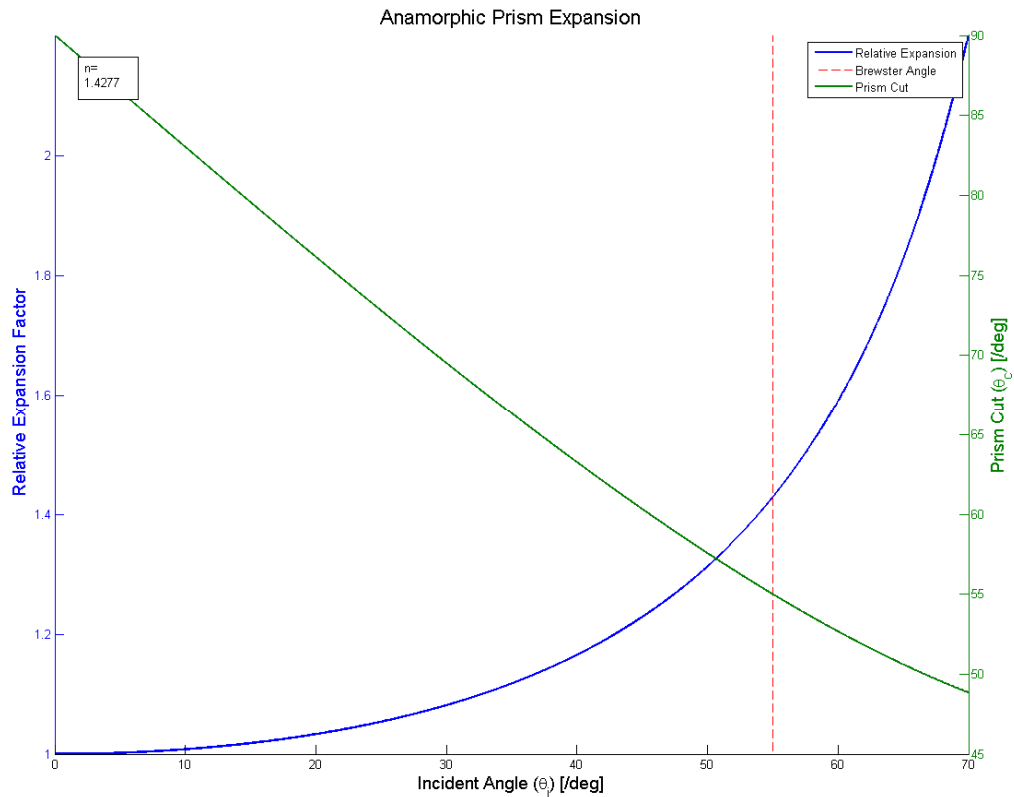


Figure 4.5.2: Relative expansion factor for a single prism at various angles of incidence for a refractive index of 1.42767.

Of course, there are a range of solutions to supply the correct expansion factor for any given set-up; initial beams size and desired final beams size, are all dependent on the desired final adjustment to the beams size. The initial beams size can be changed with a variable aperture, thereby clipping out part of the beam and energy, or the incident angle of the beam on the prism may be altered, changing the expansion factor of the prism. However this results in a loss of energy through inefficient reflections and refractions and induces ghosting throughout the entire system due to internal reflections within the prisms. This latter option also alters the final emerging beam angle from the prisms, potentially striking the plasma chamber at a non-incident angle causing further ghosting, potentially complicating the ionization process.

Method	Losses	Cost	Notes
Fixed Angle – Variable Aperture	Directly proportional to aperture size ~ 16%	Cheap	
Variable Angle – Fixed Aperture	Non-linear relationship with AR coating ~ 4%	Expensive	Ghost reflections

Table 4.5.2: Summary of anamorphic beam alteration techniques.

The required expansion factor (F_x) for any system is given by the following formula, where n = the number of prisms:

$$F_x = \sqrt[n]{\frac{d_{2max} \geq d_2 \geq d_{2min}}{d_{1max} \geq d_1 \geq d_{1min}}} \quad (4.5.8)$$

For a simple case, such a $d_2 = 8$, and $d_1 = 2$, the formula boils down into the integer n -th root of $8/2 = [4, 2, 1.5874, 1.414, \dots]$. For a more flexible scenario where the final beamsize may lie between 8 cm and 6 cm the initial beamsize may be anything ≤ 2.4 cm, the solution becomes a little bit more complex.

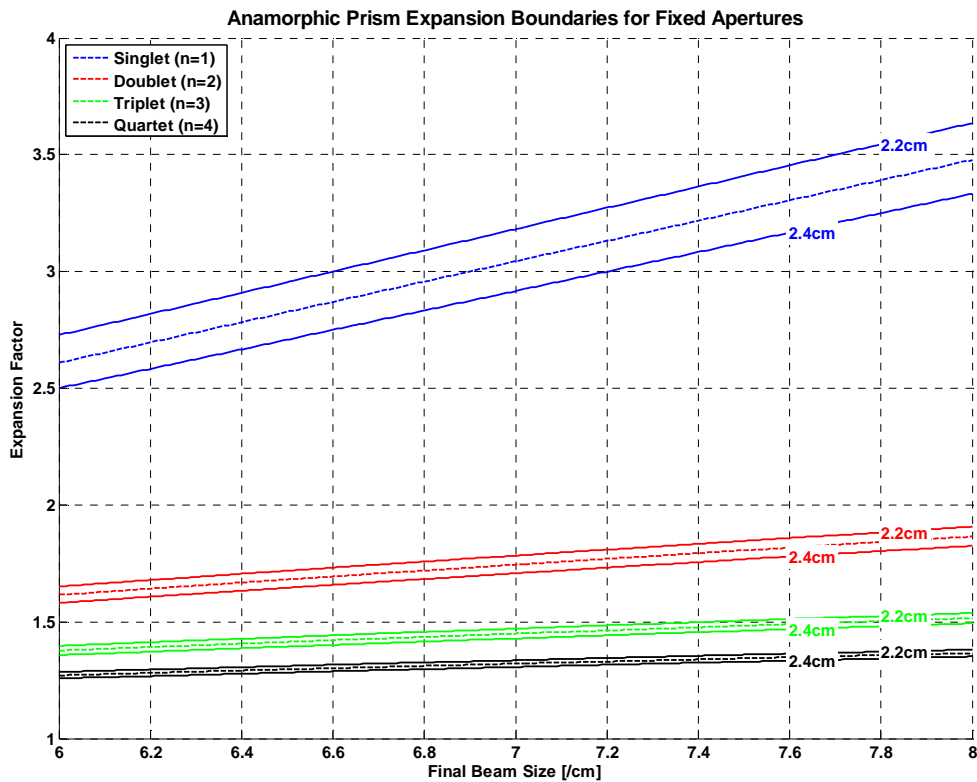
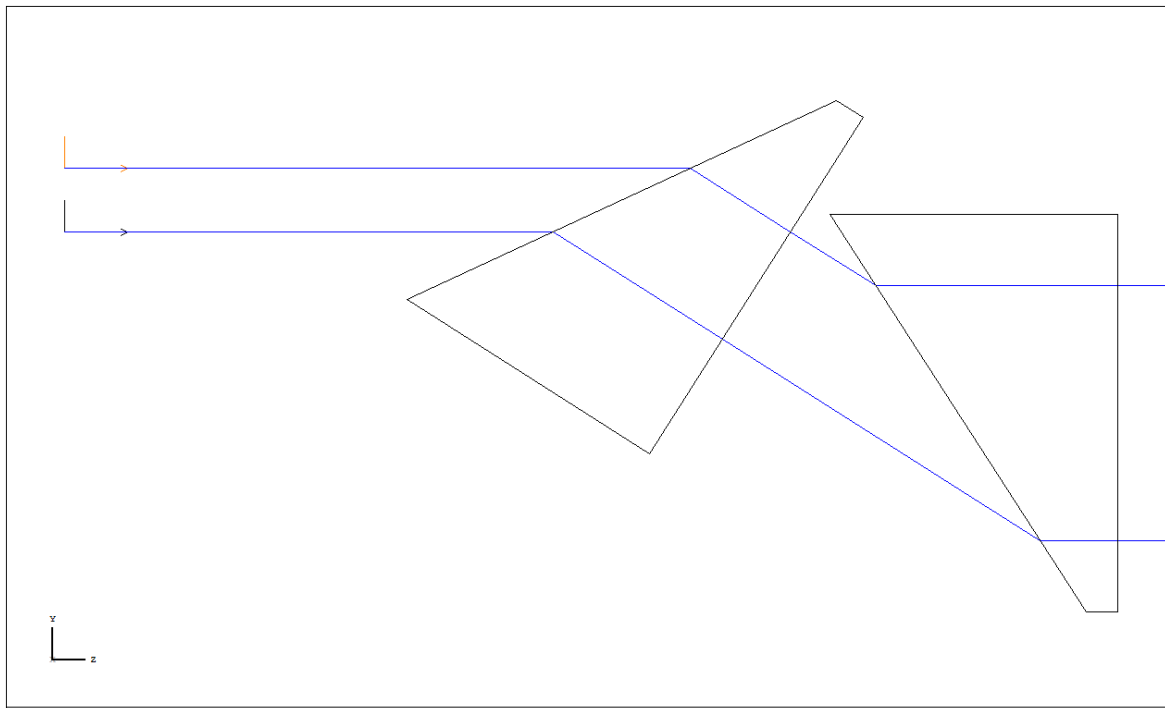


Figure 4.5.3: The expansion factor boundaries for the upper (2.4cm) and lower (2.2cm) initial beamsize limits for a variety of final beam sizes and prism multiples.

As can be seen from the graph, the amount of expansion factor range required for a fixed initial beam size, and therefore the required incident angle range, is heavily dependent on the amount of prisms. For example, the limit of a fused Silica prism doublet with the initial beamsize of 2.4 cm (solid red line), ranges between 1.581 and 1.826. This requires the incident angle to range between 59.76° and 64.97° , a total range of 5.21° . Depending on the performance of the anti-reflection coatings, this may or may not be acceptable.



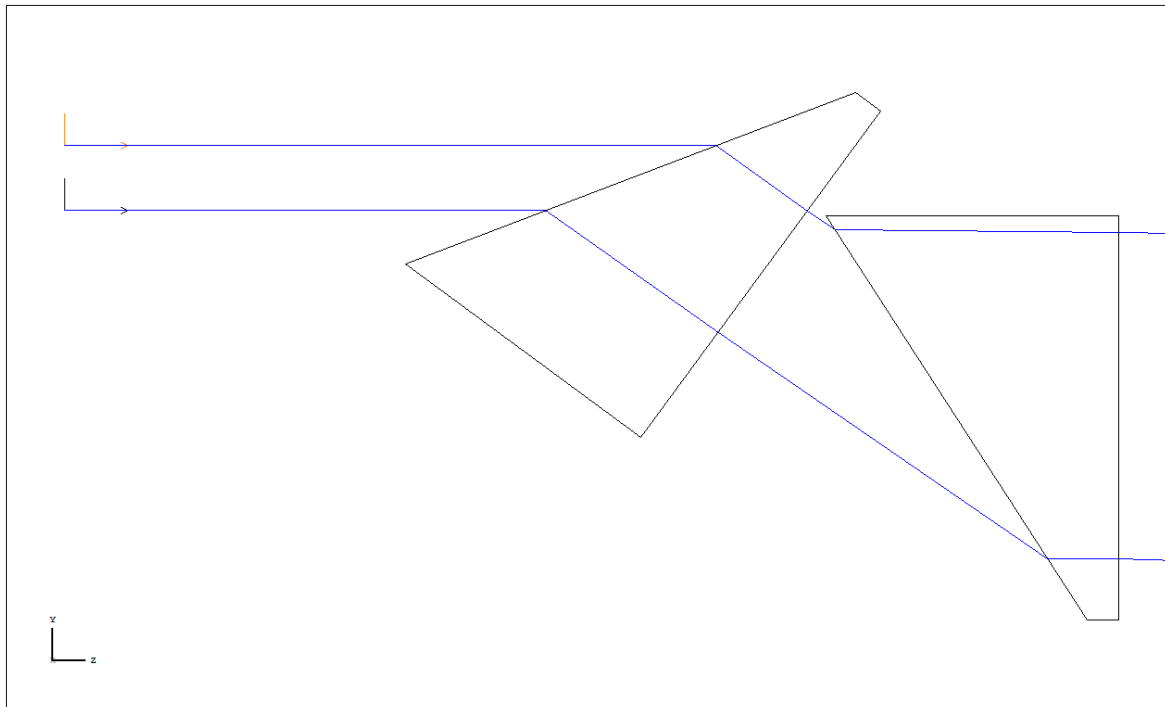


Figure 4.5.4: Comparison of a prism doublet at design incident angle and maximum incident angle. (A) $\vartheta_i = 32.345^\circ$. (B) $\vartheta_i = 36.345^\circ$.

Obviously, the amount of prisms could simply be increased to reduce the range further, but this introduces problems of its own. Increasing the amount of boundaries to reduce the incident angle range may not necessarily offset the reduced losses of the anti-reflection coatings. Also costs can quickly escalate, as sufficiently accurate precision rotational elements are costly, combined with the not inexpensive cost of the the components themselves. The difficulties are compounded as it is preferable to avoid electronics whenever possible owing to radiation-induced deterioration.

Alternatively, the incident angle may be fixed and the aperture dimension varied. The resulting beams size is given by any horizontal line and bounded by the limits of the initial beams size. For example, the final beams size of a a fixed incident angle of 60° ranges roughly between 6.1cm and 6.6cm. This can be seen below in Figure 4.5.5: The final beams size boundaries for the upper (2.4 cm) and lower (2.2 cm) limits of the initial beams size for a range of expansion factors and prism. Figure 4.5.5. As expansion factor and incident angle are related by equation (4.5.5) the expansion factor can be replotted as incident angle.

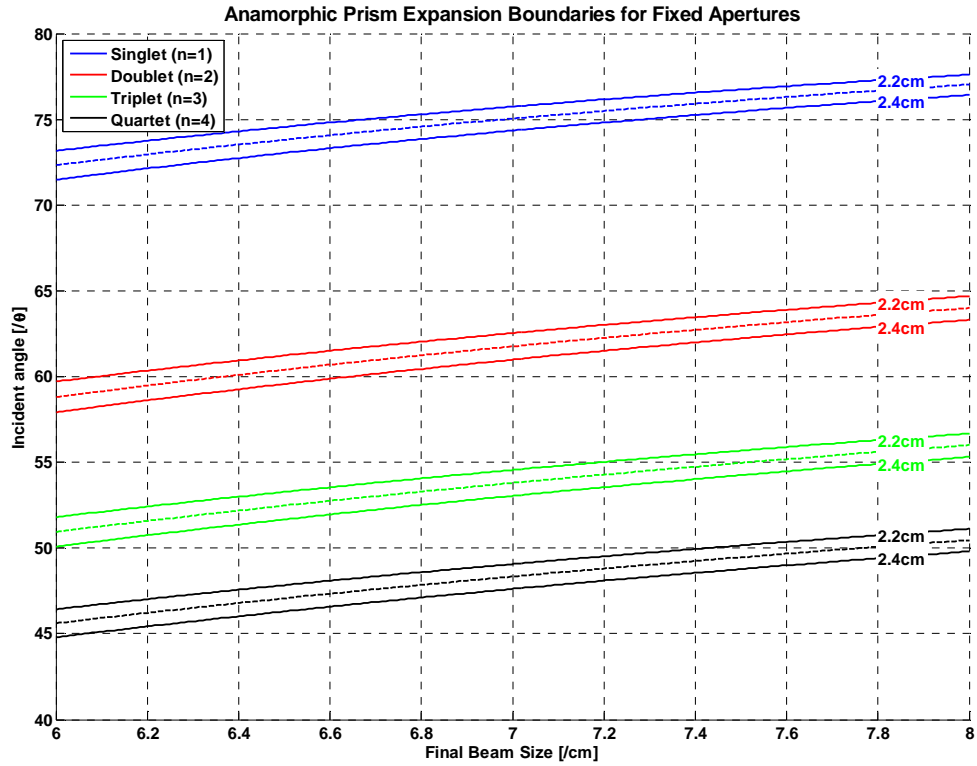


Figure 4.5.5: The final beamsizes boundaries for the upper (2.4 cm) and lower (2.2 cm) limits of the initial beamsizes for a range of expansion factors and prism.

The obvious solution is to combine both approaches, using a rotationally mounted prism pair (doublet) and a variable aperture to choose the best expansion factor. Ideally it is preferred to use prism pairs as this will only displace the beam instead of refract it at an unusual angle.

Material	n	θ_0	θ_c	Expansion Range	AOI Range	α [cm^{-1}]
MgF2	1.42767	64.22°	50.8962°	1.581 - 2	59.73° – 67.61°	0.91×10^{-3}
UV Silica (Suprasil)	1.56077	62.55°	55.349°	1.581 - 2	57.91° – 66.09°	2×10^{-3}

Table 4.5.3: Prism material design summary.

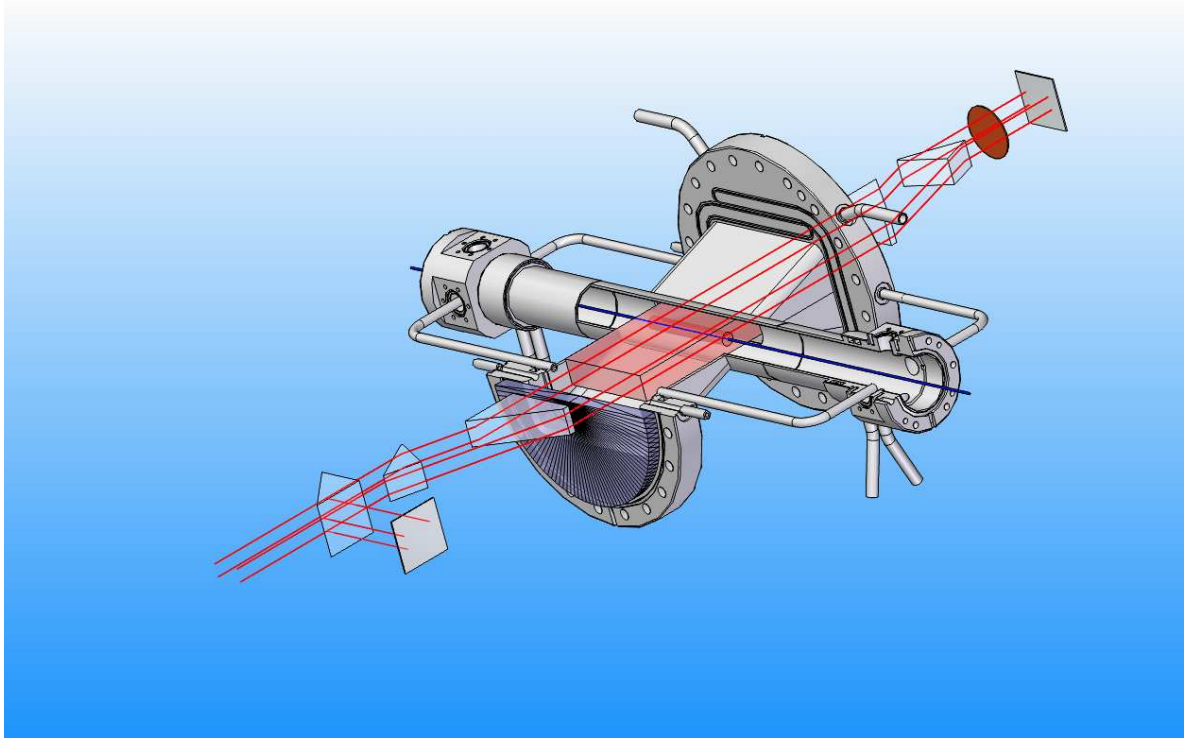


Figure 4.5.6:CAD drawing of final system.

4.6 Polarization & Birefringence

It is necessary to discuss polarization and birefringence at this point as it is a crucial aspect of the setup for the experiment. It is only by manipulation of the polarization states that the topography is viable. Polarization is the separation of the electric field of an incident beam into two orthogonal components: E_x and E_y . For unpolarized light, this is just the superposition of many waves and fields, but for lasers the beam is typically linearly polarized, and on some rare occasions circularly polarized.

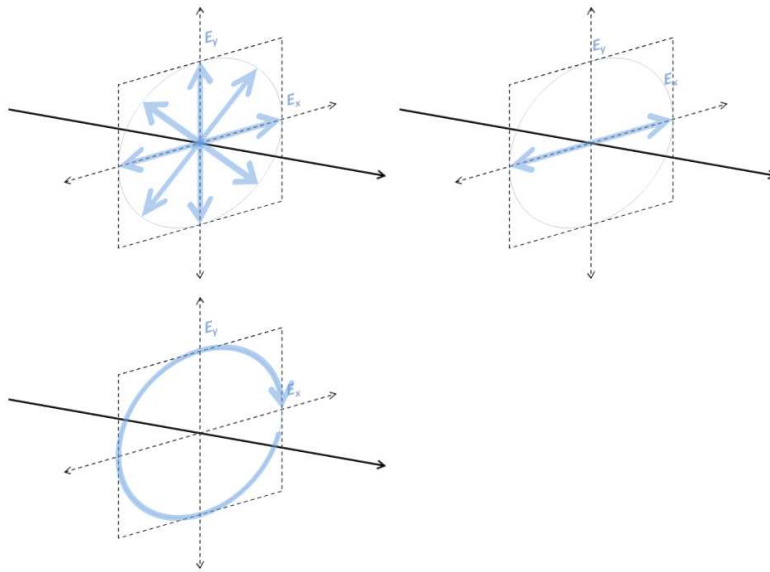


Figure 4.6.1: Unpolarised light, linearly polarized light in the horizontal direction, and right-hand circularly polarized light.

Birefringence is the double refraction of light in a material based upon the anisotropy of the material and the relative propagation direction and polarization of the light itself. Most optical materials are isotropic; the index of refraction is uniform in all directions for all polarizations. This is easily visualized for any regular crystalline solid.

For anisotropic materials, which may be uniaxial ($n_1 = n_2 \neq n_3$) or biaxial ($n_1 \neq n_2 \neq n_3$), the largest index of refraction is defined as the “optical axis”. The then perceived refractive index of a material by a light ray is dependent of the relative propagation direction of that ray within the material to this optical axis.

A simple example would be a linearly polarized ray impinging on a calcite crystal. When the ray propagates parallel to the optical axis it experiences the ‘ordinary’ refractive index of 1.658. However if the crystal is rotated 90° so that the ray is polarized in the same axis as the crystal it will experience an index of 1.486. In this manner a wave retarder can be created by the rotation of the crystal axis at 45° to linearly polarized light. If the light is considered as the composition of two orthogonal components each component will experience a different refractive index, causing one to slow relative to the other component. This induces a relative phase change (Γ) between the two components given by:

$$\Gamma = \frac{2\pi \Delta n L}{\lambda_0} \quad (4.6.1)$$

Where Δn is the birefringence, L is the path length within the material, and λ_0 is the primary wavelength.

4.7 Quarter Wave Plate

The operation of the mirror-coupled quarter waveplate can easily be confirmed with Jones matrices^{5}. There are two possible reference frames for the system: the easy way; in which we consider the light to be linearly polarized at 45° and orientate the fast-axis of the quarter-waveplate vertically or horizontally, or the hard way; in which we consider the light linearly polarized vertically or horizontally and rotate the fast-axis of the QWP 45° with respect to this. Fortunately Matlab's symbolic toolbox can be used to easily solve these matrices.

Jones matrices solution for linearly polarized light at $+45^\circ$ from x-axis:

$$\begin{bmatrix} 1 & 0 \\ 0 & -i \end{bmatrix} \frac{1}{\sqrt{2}} \begin{bmatrix} 1 \\ 1 \end{bmatrix} = \frac{1}{\sqrt{2}} \begin{bmatrix} 1 \\ -i \end{bmatrix} \quad \dots RHP \quad (4.7.1)$$

$$\begin{bmatrix} 1 & 0 \\ 0 & -1 \end{bmatrix} \frac{1}{\sqrt{2}} \begin{bmatrix} 1 \\ 1 \end{bmatrix} = \frac{1}{\sqrt{2}} \begin{bmatrix} 1 \\ i \end{bmatrix} \quad \dots LHP \quad (4.7.2)$$

$$\begin{bmatrix} 1 & 0 \\ 0 & -i \end{bmatrix} \frac{1}{\sqrt{2}} \begin{bmatrix} 1 \\ i \end{bmatrix} = \frac{1}{\sqrt{2}} \begin{bmatrix} 1 \\ 1 \end{bmatrix} \quad \dots LP \quad (4.7.3)$$

It must be noted however, that the answer is always in the reference frame of the beam, which now has an inverse k vector, which is the mirror opposite of the original frame.

Jones matrices solution for linearly polarized light on the x-axis, where $\theta = 45^\circ$:

$$\begin{bmatrix} \cos(\theta) & -\sin(\theta) \\ \sin(\theta) & \cos(\theta) \end{bmatrix} \begin{bmatrix} 1 & 0 \\ 0 & -i \end{bmatrix} \begin{bmatrix} \cos(-\theta) & -\sin(-\theta) \\ \sin(-\theta) & \cos(-\theta) \end{bmatrix} \begin{bmatrix} 1 \\ 0 \end{bmatrix} = \frac{1}{\sqrt{2}} \begin{bmatrix} 1 \\ -i \end{bmatrix} \quad \dots RHP \quad (4.7.4)$$

$$\begin{bmatrix} 1 & 0 \\ 0 & -1 \end{bmatrix} \frac{1}{\sqrt{2}} \begin{bmatrix} 1 \\ 1 \end{bmatrix} = \frac{1}{\sqrt{2}} \begin{bmatrix} 1 \\ i \end{bmatrix} \quad \dots LHP \quad (4.7.5)$$

$$\begin{bmatrix} \cos(-\theta) & -\sin(-\theta) \\ \sin(-\theta) & \cos(-\theta) \end{bmatrix} \begin{bmatrix} 1 & 0 \\ 0 & -i \end{bmatrix} \begin{bmatrix} \cos(\theta) & -\sin(\theta) \\ \sin(\theta) & \cos(\theta) \end{bmatrix} \frac{1}{\sqrt{2}} \begin{bmatrix} 1 \\ i \end{bmatrix} = \begin{bmatrix} 0 \\ 1 \end{bmatrix} \quad \dots LP \ 90^\circ \quad (4.7.6)$$

It must be remembered, in the rotated element case, that the rotated fast axis of the waveplate is the mirror opposite on the return path; what was $+45^\circ$ now becomes -45° .

^{5} Footnote 9.5: Jones Matrices

4.8 Beamsplitters Overview

4.8.1 Overview

There are many types of polarizers on the market. Starting with simple polarizers such as the absorptive dichroic polarizer originally invented by E. Land (of Polaroid fame) in 1928 (20) or the wire grid polarizers used in the high-power vis-IR spectrum. There are beamsplitting polarizers, such as the “pile of plates” setup invented by Arago in 1812 (21), where a series of windows or plates are set at the Brewster angle to transmit the p-polarized light and sequentially reflect a fixed amount of the s-polarized light per interface. The disadvantage of the final arrangement is the broadening of the reflected component.

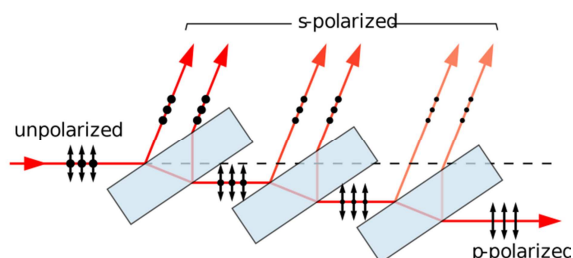


Figure 4.8.1.1: “Pile of plates” polarizer.

This concept can naturally be improved by exploiting modern thin-film deposition techniques; in essence creating a compressed “pile of plates”, thereby negating the broadening of the reflected component. MacNeille refined this idea in 1946 to design thin-film cube beamsplitters (22), where alternating high- and low-index film layers are sandwiched between two prisms, which is the basis for most modern polarizing beamsplitters. In this work “thin-film” and “MacNeille” shall be used interchangeably, as conceptually there is little difference between the two, that is, a MacNeille could just as easily be sandwiched between a substrate and a protective coating.

Finally, there exists birefringent beamsplitters, where the orthogonally polarized components experience different refractive indices and subsequently alternate optical paths, or “walk-off”.

Given the requirement to retain the rotationally polarized beam only the latter two options are possibilities. The MacNeille beamsplitter is the preferred option, as it promises greater performance owing to the thinness of the device, and high extinction-ratios can be achieved with suprisingly few layers. The birefringent prism is the backup option as the designs are limited by available materials; few birefringent materials exist that are suitably transmissive at 193nm and those that do must be optically contacted as there is no optical glue available at this wavelength to cement the prism together.

4.8.2 MacNeille polarizer

The thin-film concept behind the MacNeille beamsplitter is quite fundamental; alternating layers of high- and low-index optical material are deposited on a substrate. Where $n_1 \gg n_2$, and $n_1 > n_3$. Like the “pile of plates” all internal angles of incidence are at the Brewster angle, and all partially reflected rays are completely s-polarized.

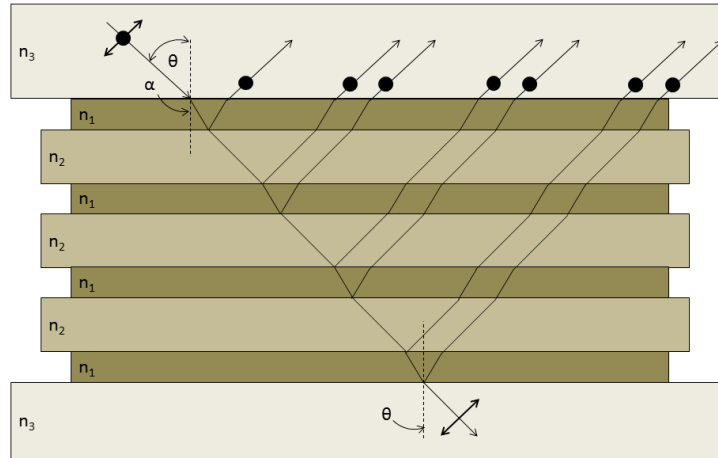


Figure 4.8.2.1: MacNeille thin-film polarizer.

For example, letting $n_1 = 3.4$ (Barium Titante), and $n_2 = 1.43$ (Magnesium Flouride) the Brewster angles are therefore:

$$\alpha = \text{atan}\left(\frac{1.43}{3.4}\right) = 23^\circ \quad (4.8.2.1)$$

$$\alpha = \text{atan}\left(\frac{3.4}{1.43}\right) = 67^\circ \quad (4.8.2.2)$$

And we can easily choose the refractive index or incident angle from Snell's law:

$$n_3 \sin(\theta) = n_1 \sin(\alpha) \quad (4.8.2.3)$$

We can choose the incident angle to be 45° , giving us a necessary refractive index for n_3 of 1.88, or we could select a refractive index such as 1.92 (Barium Borate) and determine the incident angle to be 43.8° . Additionally, we can control the thickness of the layers to cause constructive interference, maximizing our outputs. Then the thicknesses need only be:

$$t_{n_1} = \frac{\lambda}{4\sqrt{(n_1^2 + n_2^2)/n_1^2}} \quad (4.8.2.4)$$

$$t_{n_2} = \frac{\lambda}{4\sqrt{(n_1^2 + n_2^2)/n_2^2}} \quad (4.8.2.5)$$

In the example given above, the calculated Fresnel reflections between each $n_1:n_2$ interface is approximately 50%. With six interfaces alone the amount of transmitted s-polarized light is approximately 1.5%. Clearly, the achievable extinction ratio with even such a basic MacNeille polarizer are incredible. This performance comes at high cost, however. A custom 2" splitter costs approx. USD\$4000, although the majority of this cost is tooling.

4.8.3 Birefringent Polarizer

This difference in refractive index for polarization components can traditionally be exploited to produce many variants of polarizing beamsplitters. Such as the Calcite-based Glan family of prisms which exploits birefringence to cause total internal reflection for one polarization (Figure 4.8.3.1):

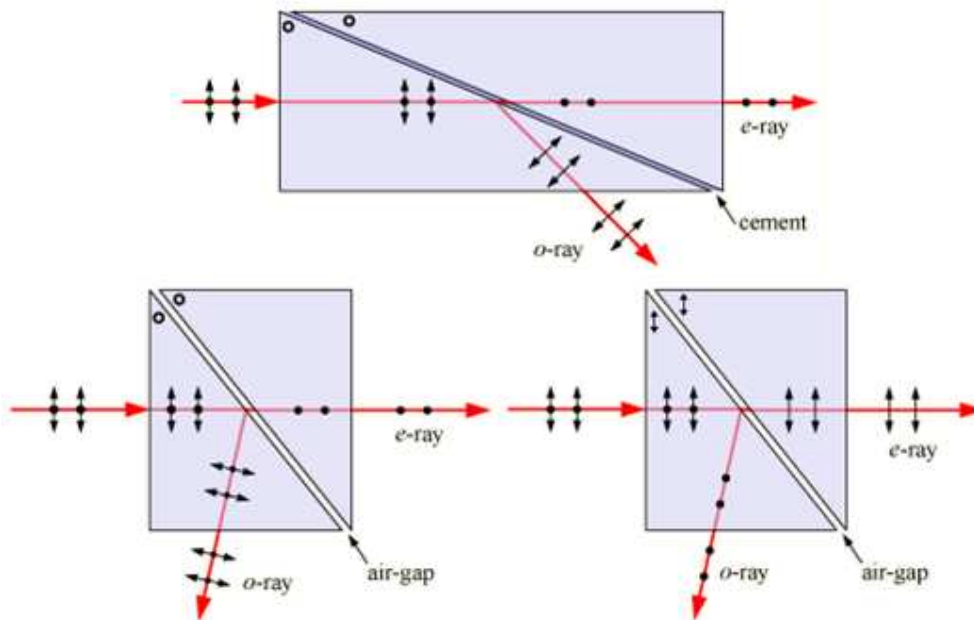


Figure 4.8.3.1: Overview of the Glan family of birefringent prisms which reflect the extraordinary ray.

Or the family of birefringent polarizers (Sénarmont, Rochon, Wollaston) which refract the polarized components in different directions:

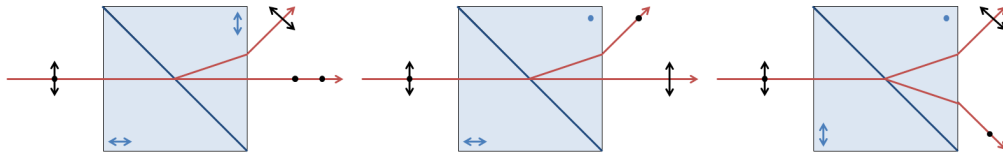


Figure 4.8.3.2: Overview of birefringent polarizers which refract the extraordinary ray.

However, the lack of birefringent materials with sufficient transmissibility at 193nm, the lack of suitable optical cement at this wavelength, and the relatively high power of the laser drastically restrict potential designs to only those which may be optically contacted or air-gapped.

As far as can be ascertained, the only commercially available polarizers in the VUV are Rochon-based. The supposition is that this is the only applicable design for the available birefringent materials. Those that are available are typically made of Quartz or Magnesium Fluoride (MgF₂). These typically have a divergence angle of 2.5° - 4°. Given that a typically “large” MgF₂ Rochon polarizer has a circular aperture of only 12 mm, and the desired displacement of the beam is at least 1.5x that of the beamsize, the minimum optical path length is given by:

$$l = \frac{1.5 \cdot d_1}{\tan(\theta)} \quad (4.8.3.1)$$

Where $d_1 = \sqrt{\frac{\phi^2}{2}}$, and $\phi = 12\text{mm}$

$$l = \frac{1.5 \cdot 8.5\text{mm}}{\tan(\theta)} \quad (4.8.3.2)$$

$$l = \frac{1.5 \cdot 8.5\text{mm}}{\tan(2.5)} = 29.2\text{cm} \quad l = \frac{1.5 \cdot 8.5\text{mm}}{\tan(4)} = 18.2\text{cm} \quad (4.8.3.3)$$

While these distances are not unreasonable, the small aperture diameter would mandate another set of expansion/compression prisms in order to get the beam from its original size to 8.5mm; introducing further loss mechanisms into the system.

In summary, while the Rochon polarizers are cheaper at \$1800 each, this cost reduction is offset by the requirement of additional prisms. The MacNeille polarizer is clearly the superior choice when the absorption of the polarizers is compared: ~3% and ~12%.

4.8.4 Conceptual Experiment

To test the concept the photo-cathode laser for the PITZ accelerator was used. It is a 257nm frequency quadrupled Yb:YAG laser used for the generation of the electron bunches within the accelerator. While the wavelength, lying deep in the UV, is close to the target wavelength, the power is significantly smaller on the order of mW.

The laser was set up as much like Figure 4.4.1: a quarter-waveplate for the 266 nm was used, a polarizing beamsplitter cube, and a powermeter placed at the orthogonal output of the cube. The waveplate was then manually rotated about its axis by 2° steps and the power recorded. The raw data was then plotted:

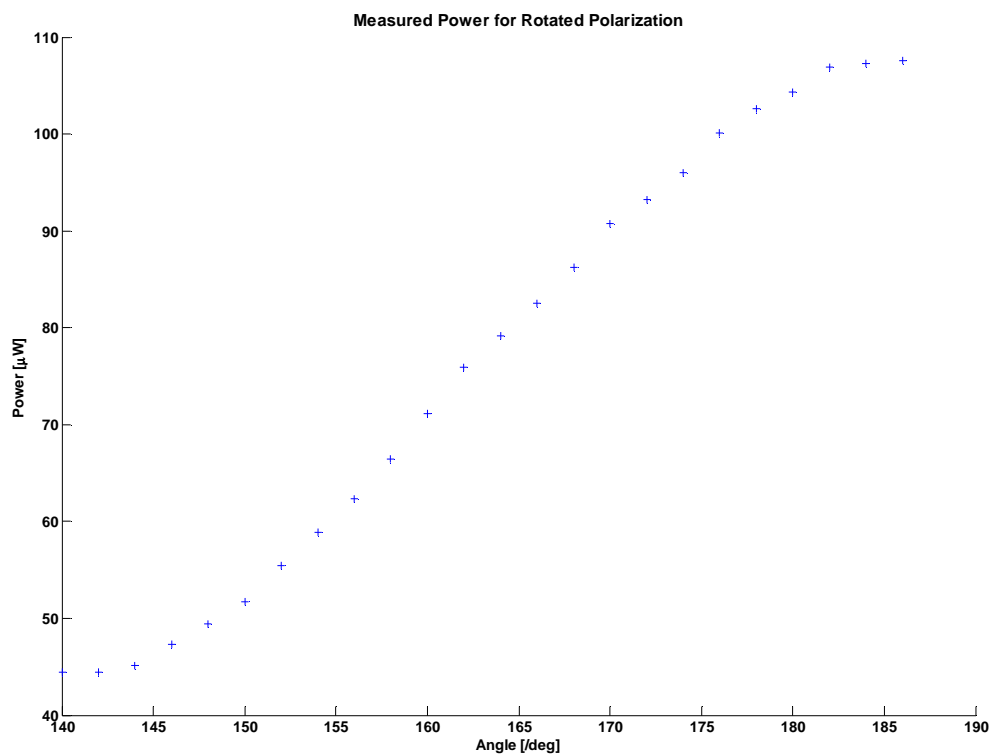


Figure 4.8.4.1: Recorded reflected power for an optical isolator as a function of rotated quarter waveplate.

As can be seen, the recorded power increases from a minimum, presumably background level, sinusoidally up to a maximum 45° later; from ~45 μW to ~108 μW.

5 Further Experimental Proposals

5.1 Pockels Cell Research

As far as can be ascertained there are no conclusive studies in literature as to the operation of electro-optic components in the vacuum ultraviolet. There is some interest in industry on this topic, consequently it is proposed to perform materials testing on potential candidates for a Pockel cell at 193 nm. To which a sample of BBO, ADP, KDP, and KDKP Pockel cells would be mounted unto a Peltier cell and the half-wave voltage and transmission determined for each sample as a function of temperature – particularly sub-zero temperatures. Therefore the samples would be mounted into a N_2 or vacuum environment as to inhibit the condensation of atmospheric water vapour, and to prevent the destruction of some of the water-soluble materials

5.2 Plasma Probe

For the initial out-of-beamline plasma generation experiments it is planned to use a portion of the ionizing excimer laser beam as a 'probe' to co-calibrate the plasma density measurements obtained from interferometry. The Fresnel reflections from a sub-mm thick microscope cover slip can be used to divert a fixed percentage of the initial beam prior to ionization depending on the wavelength-dependent refractive index of the cover slip.

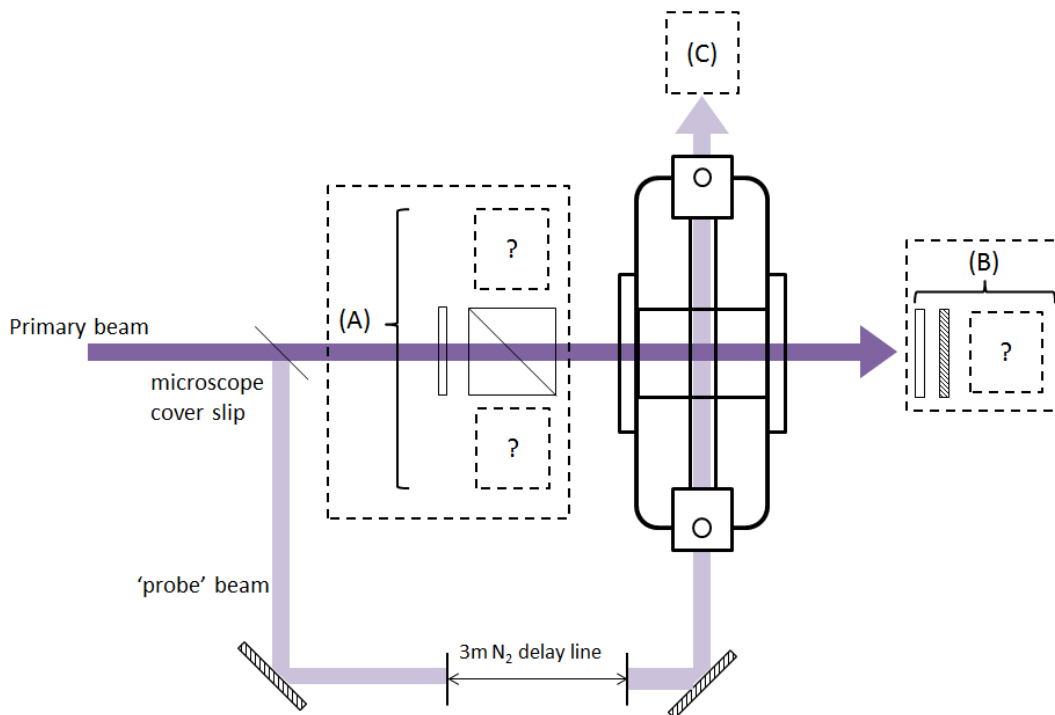


Figure 5.2.1: A schematic overview of the proposed vapour:plasma density measurement calibration scheme. (A), (B), or (C) can be any combination of beamstops, powermeters, or (polarization-rotating) reflective optics.

Given the nominal thickness of $150\ \mu\text{m}$ for a typical cover slip, glasses typically highly attenuating in the VUV, such as BK7, may be used owing to the negligible absorption; even

for a high attenuation coefficient such as 2 cm^{-1} the absorption is only 3%. Any path deviations may also be ignored.

As the laser is polarized the fixed reflectance may be initially “chosen” by rotating the slip by 90° and designing the optical layout for that orientation, or by half-wave plates. For example, for BK7⁽⁶⁾ the reflectance may be selected to be either $\sim 3.2\%$ (p-pol) or $\sim 25.4\%$ (s-pol).

Naturally, the ‘probe’ beam must arrive after the ionization beam and so must be delayed. The $>3 \text{ m}$ delay line must be housed in a N_2 environment to prevent absorption of the beam by atmosphere and the production of ozone.

Before injection into the plasma cell a half-wave plate combined with the polarizing beamsplitter at (A) can be used to vary the energy of the ionization beam between 0% and 100%. By altering the polarization of the beam it can be completely deflected, partially deflected, or completely transmitted by the beamsplitter. The ‘probe’ beam can then be set as a fixed percentage of the initial beam, while the energy of the ionization beam can be completely varied.

After a single pass through the plasma cell, the beam may then have its polarization rotated and reflected back at (B), or the energy could be measured by a powermeter, or absorbed by a beamdump depending on preference.

Of course the energy of the ‘probe’ beam must be measured, so a powermeter would be placed at (C).

Given a similar buffer zone ratio as per Muggli et. Al of 1:3:1, a dimensionally unmodified ionizing laser beam, and assuming the Beer-Lambert exponential absorption then the path of the probe beam should look like:

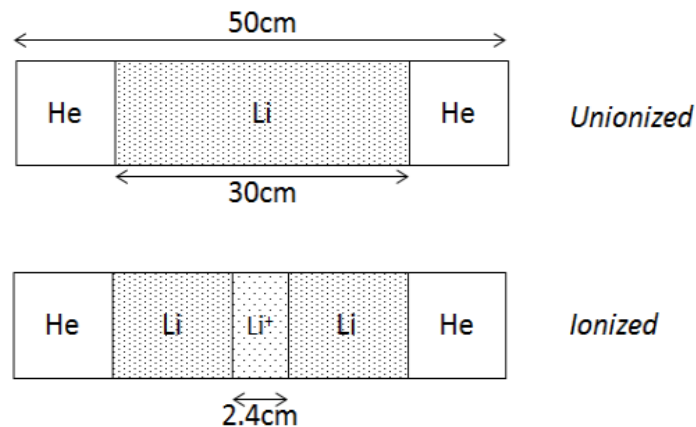


Figure 5.2.2: Approximate path layout experienced by the ‘probe’ beam for

⁽⁶⁾ Footnote 9.6: Fresnel Plots for Various Materials at 193 nm

The plasma density in the system can be predicted by the energy difference at the powermeter between the ionized state and unionized state:

$$\Delta E = E_{ionized} - E_{unionized} \quad (5.2.1)$$

Where σ is the atomic cross-section, N_v is the number of species per cm^3 in the vapour column, and l is lateral length of the vapour column:

$$E_{unionized} = e^{-\sigma N_v l} \quad (5.2.2)$$

Where N_p is the number of electrons per cm^3 in the ionized column, and x is the lateral length of the ionized column:

$$E_{ionized} = e^{-\sigma N_v(l-x)} e^{-\sigma(N_v-N_p)x} \quad (5.2.3)$$

$$E_{ionized} = e^{-\sigma N_v l} e^{\sigma N_p x} [e^{\sigma N_v x} e^{-\sigma N_v x}] \quad (5.2.4)$$

$$E_{ionized} = e^{-\sigma N_v l} e^{\sigma N_p x} \quad (5.2.5)$$

Therefore:

$$\Delta E = e^{-\sigma N_v l} e^{\sigma N_p x} - e^{-\sigma N_v l} \quad (5.2.6)$$

$$\Delta E = e^{-\sigma N_v l} (e^{\sigma N_p x} - 1) \quad (5.2.7)$$

The plasma density after one pass through the system with a pulsetrap topography is given by:

$$N_p = \frac{(E_{pulse} - losses) \left[e^{-\sigma N_v (\frac{w}{2} - 0.5)} - e^{-\sigma N_v (\frac{w}{2} + 0.5)} \right]}{E(\lambda)} \quad (5.2.8)$$

where E_{pulse} is the energy of the laser pulse, w is the lateral width of the vapour column, and $E(\lambda)$ is the photon energy as a function of wavelength.

The signal magnitude as a percentage of probe pulse energy can then be plotted as a function of vapour density. Where $\sigma = 0.018 \text{ cm}^{-2}$, $\lambda = 193 \text{ nm}$, $w = 16 \text{ cm}$, and $E_{pulse} = 0.05 \text{ J}$:

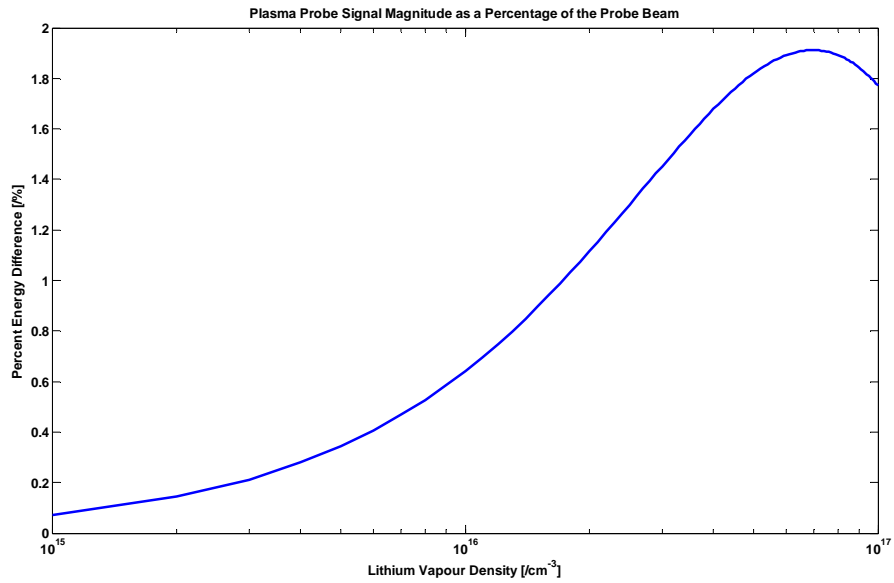


Figure 5.2.3: Probe signal as a percentage energy difference of the probe pulse energy as a function of Lithium for a typical pulsetrap system.

As would be expected the probe signal follows a similar shape as the plasma density map (Figure 4.2.5) and what the signal magnitude may be for given system parameters.

6 Conclusion

The nuances of the problem were thoroughly reviewed and a range of solutions presented based on two possible methods. For direct ionization multi possible topographies were conceived, and three thoroughly simulated through Zemax and Matlab. The relative merits and flaws of beamfolder, butterfly, and pulsetrap topographies were discussed, and an appropriate topography selected.

Field ionization was also reviewed. The schematic merits compared to the spatial and practical limits set by the requirements of the PITZ beamline and budget. Since the method was impractical in this scenario potential solutions were proposed. These proposals were to construct graded-index lenses or modify the local angle of incidence to reduce the lateral length while potentially maintaining or increasing the beam width.

For the selected design, the pulsetrap, potential candidates for an electro-optic element (Pockels cell) and polarizer were researched. An appropriate compromise for the electro-optic element was made via a waveplate. The system was then designed about the requirements for the plasma and the technicalities of the laser system that would be available.

Prisms for anamorphic expansion of the laser beam were designed and ordered, Magnesium Fluoride windows were sourced, a custom design for a MacNeille thin-film polarizer at 193 nm was commissioned and ordered, and the mirrors and waveplates sourced from vendors.

The concept was tested locally and shown to be in agreement with theory. Further research, calibration, and confirmation experiments were proposed with some interest from industry on the former.

Overall, the concept of a polarization-based pulse trap is sound and robust, and potentially very scalable for alternative scenarios where the attenuation is not such an issue.

7 Bibliography

1. *Laser Electron Accelerator*. **Tajima, Dawson**. 4, 1979, Phys. Rev. Lett., Vol. 43, pp. 267-270.
2. *Photo-Ionized Lithium Source for Plasma Accelerator Applications*. **Muggli, P.** 1999, IEEE TRANSACTIONS ON PLASMA SCIENCE, p. 791.
3. **(Eds.), Martienssen and Warlimont**. *Springer Handbook of Condensed Matter and Materials Data*. s.l. : Springer, 2005.
4. *Plasmas, Dielectrics and the Ultrafast: First Science and Operational Experience at FACET*. **al., Clarke et.** Tel Aviv : s.n., 2012. 26th International Linear Accelerator Conference (LINAC12) .
5. *The Photoionization Absorption Continua for Alkali Metal Vapours*. **Creek, Marr and.** 1477, April 1968, Proc. R. Soc. Lond. A, Vol. 304, pp. 233-244.
6. *Atomic Absorption Cross Sections of Lithium and Sodium Between 600 and 1000Å*. **Hudson, Carter and.** 5, J. Opt. Soc. Am., Vol. 57, pp. 651-654.
7. **Del Mar Ventures**. LG105 Fifth Harmonic Generator for Nd:YAG Lasers User's Manual. [Online] http://www.dmphotronics.com/NdYAG_laser_harmonics_OPO_Raman_Shifter/Fifth-Harmonic-Generator-NdYAG-laser-LG105-manual.pdf.
8. *Preparations for a plasma wakefield acceleration (PWA) experiment at PITZ*. **Gross**. 2013, Nuclear Instruments and Methods in Physics Research Section A.
9. **Eberly, Milonni and.** Single-mode Fibers. *Laser Physics*. 2. s.l. : Wiley, 2010, p. 363.
10. *Empirical formula for static field ionization rates of atoms and molecules by lasers in the barrier-suppression regime*. **Tong, Lin**. 15, 2005, Journal of Physics B, Vol. 38.
11. *High quality quasi-Bessel beam generated by round-tip axicon*. . **Brzobohatý O, Cizmár T, Zemánek P**. 2008, Optics Express, pp. 12688-12700.
12. *UV-visible Faraday rotators based on rare-earth fluoride single crystals: LiREF₄ (RE = Tb, Dy, Ho, Er and Yb), PrF₃ and CeF₃*. **Valentyn Vasylyev, Encarnación G. Villora, Masaru Nakamura, Yoshiyuki Sugahara, and Kiyoshi Shimamura**. 13, 2012, Optics Express, Vol. 20, pp. 14460-14470.
13. *Attaining 186-nm light generation in cooled b-BaB₂O₄ crystal*. **Kuwano, Kouta and.** 17, s.l. : Optics Letters, 1999, Vol. 24.
14. *KDP and ADP transmission in the vacuum ultraviolet*. **Smith, W. Lee**. 7, s.l. : Applied Optics, 1977, Vol. 16.
15. *Linear electrooptic effect in doped KDP crystals*. **Varma, Ramanaiah, Veerabhadra Rao**. 1, March 1983, Bulletin of Materials Science, Vol. 5, pp. 39-48.
16. *Temperature dependences of the electro-optic coefficient in DKDP crystal*. **Y. Takeuchi, A. Yoshida, S. Tokita, M. Fujita, J. Kawanaka**. Seoul : s.n., 2007. Lasers and Electro-Optics - Pacific Rim, 2007. CLEO/Pacific Rim 2007. Conference on. pp. 1 - 2.

17. *Ultraviolet electro-optic amplitude modulation in β -BaB₂O₄ waveguides*. **al, R. Degl'Innocenti et.** s.l. : Appl. Phys. Lett, 2007, Vol. 91.
18. *Design and manufacture of a gradient-index axicon*. **Fischer, Hardrider, Moore.** 16, 2000, Applied Optics, Vol. 39, pp. 2687 - 2694.
19. **Metzger, Robert M.** *The Physical Chemist's Toolbox*.
20. **Land.** *Polarizing refracting bodies*. 1,918,848 US, 1929.
21. **Band, Y. B.** *Light and Matter: Electromagnetism, Optics, Spectroscopy and Lasers*. 2007. p. 140.
22. **MacNeille, S. M.** *Beam Splitter*. 2,403,731 US, 1946.

8 Table of Figures

Figure 1.1: A conceptual overview of the prototype plasma cell and placeholder optics.....	3
Figure 1.2: Field ionization potentials for different electric field gradients.....	4
Figure 2.1.1: Conceptual overview of the nonlinear absorption of the Lambert-Beer law.	6
Figure 2.2.1: Gaussian beam overview.	7
Figure 2.2.2: Focussing of Gaussian beam within plasma cell.	8
Figure 2.2.3: Bessel beam projected into plasma cell.	8
Figure 3.1.1: Schematic overview of a beam-folding topography. The plane mirrors are above and below the volume – the end mirrors are marked with 1, 2 and 3.	9
Figure 3.2.1: Overview of a seven-pass multipass topography.....	10
Figure 3.3.1: Conceptual overview of a pulsetrap.	10
Figure 3.4.1: Bessel beam formation by a perfect axicon from a Gaussian beam. (11)	13
Figure 3.4.2: Radial intensity distribution for a Bessel beam with a FWHM of 3.3 mm.	14
Figure 3.4.3: Lobe width (b_0) and focal distance (z_{max}) of an axicon-generated Bessel beam for an incident beam of 780 nm and a refractive index of 1.5.	15
Figure 3.4.4: A typical axicon and a GRIN-modified axicon.....	15
Figure 4.1.1: Geometrically idealized layout of the beamfolder used to illustrate the concept, simulated in Zemax.	17
Figure 4.1.2: The absorbed flux in the detector volume of an idealized beamfolder with indicative ‘hot’ and ‘cold’ spots.	18
Figure 4.1.3: Fully modelled beamfolder with illustrative ‘gaps’ and an order of magnitude difference in absorbed flux.....	18
Figure 4.1.4: Schematic overview of a five-pass resonator in Zemax.	19
Figure 4.1.5: Fluxes through the Lithium volume for the five-pass multipass configuration.	20
Figure 4.1.6: Conceptual simulation of a passive-pulsetrap in Zemax.....	21
Figure 4.1.7: Zemax simulations of the passive pulsetrap.	22
Figure 4.2.1: Overview of the simplified, linear system modelled in Matlab.	23
Figure 4.2.2: Example Beer-Lambert absorption curve quantized into voxels.	23
Figure 4.2.3: Lateral plasma density with each pass through an arbitrary system.....	24
Figure 4.2.4: Visual representation of the ‘slicing’ and discretization of the vapour volume for simulation. (A) System overview. (B)The plasma chamber is removed. (C) The vapour volume “sliced”. (D) The slice discretized.....	25
Figure 4.2.5: Plasma density surface map for a centrally located voxel in a Lithium vapour with an arbitrary laser energy, system length, and system losses.....	27
Figure 4.2.6: Temporal overview of a pulsetrap.	28
Figure 4.3.1: Idealized longitudinally ionizing plasma generation.	29
Figure 4.3.2: Schematic overview of a symmetric pulsetrap for long, on-axis plasma generation.	30
Figure 4.3.3: Plasma density for a longitudinally ionized two-pass passive pulsetrap.....	31
Figure 5.1.1: Conceptual schematic of a Poor-man’s optical isolator.....	32
Figure 5.2.1: Schematic overview of a prism expander	33
Figure 5.2.2: Relative expansion factor for a single prism at various angles of incidence for a refractive index of 1.42767.....	34
Figure 5.2.3: The expansion factor boundaries for the upper (2.4cm) and lower (2.2cm) initial beamsizes limits for a variety of final beam sizes and prism multiples.....	36

Figure 5.2.4: Comparison of a prism doublet at design incident angle and maximum incident angle. (A) $\theta_i = 32.345^\circ$. (B) $\theta_i = 36.345^\circ$	37
Figure 5.2.5: The final beamsizes boundaries for the upper (2.4 cm) and lower (2.2 cm) limits of the initial beamsizes for a range of expansion factors and prism.	38
Figure 5.2.6: CAD drawing of final system.	39
Figure 5.3.1: Unpolarised light, linearly polarized light in the horizontal direction, and right-hand circularly polarized light.	40
Figure 5.5.1.1: "Pile of plates" polarizer.....	42
Figure 5.5.2.1: MacNeille thin-film polarizer.....	43
Figure 5.5.3.1: Overview of the Glan family of birefringent prisms which reflect the extraordinary ray. .	44
Figure 5.5.3.2: Overview of birefringent polarizers which refract the extraordinary ray.....	45
Figure 5.5.4.1: Recorded reflected power for an optical isolator as a function of rotated quarter waveplate.	46
Figure 6.2.1: A schematic overview of the proposed vapour:plasma density measurement calibration scheme. (A), (B), or (C) can be any combination of beamstops, powermeters, or (polarization-rotating) reflective optics.	47
Figure 6.2.2: Approximate path layout experienced by the 'probe' beam for	48
Figure 6.2.3: Probe signal as a percentage energy difference of the probe pulse energy as a function of Lithium for a typical pulsetrap system.....	50

9 Footnotes

9.1 Table of Alkali Metals

Atomic No. (Z)	Name	Ionization Energy [eV]	Ionization Wavelength [nm]	Melting Point [K]	Boiling Point [K]
3	Lithium	5.4	230	454	1615
11	Sodium	5.14	241	371	1156
19	Potassium	4.34	286	337	1032
37	Rubidium	4.2	295	312	961
55	Cesium	3.89	319	302	944
87	Francium*	4.07	305	300	905

*Radioactive; $T_{1/2} = 20$ min.

9.2 Table of Excimer Lasers

Gaseous Mixture	Fundamental Wavelength [nm]
XeCl	308
KrF	248
ArF	193
F ₂	157

9.3 Preliminary Calculation of Solid-State Laser Energy

For a $6 \text{ cm} \times 1 \text{ cm}^2$ volume of plasma of density 10^{15} cm^{-3} , given that one ionization event is $\sim 10^{-18} \text{ J}$ the minimum required pulse energy is:

$$6 \text{ cm}^3 \cdot 10^{15} \text{ cm}^{-3} \cdot 10^{-18} \text{ J} = 6 \text{ mJ}$$

Assuming a 10% ionization rate and 20% efficiency of the generation of the fifth harmonic:

$$6 \text{ mJ} \cdot 10 \cdot 5 = 300 \text{ mJ}$$

But that is for ionizing **only** the column of interest. If the entire lateral volume must be ionized the column can be treated as one slice of 16:

$$6 \text{ mJ} \cdot 16 \cdot 10 \cdot 5 = 4.8 \text{ J}$$

Or, more conservatively, using the utilized ArF excimer pulse of 400mJ:

$$400 \text{ mJ} \cdot 5 = 2 \text{ J}$$

9.4 Solving Prism Amplification Factor for θ

$$F_x = \frac{1}{\cos \theta} \cos \left[\sin^{-1} \frac{\sin \theta}{n} \right] \quad (9.4.1)$$

$$\dots \cos(\sin^{-1} x) = \sqrt{a - x^2} \quad (9.4.2)$$

$$F_x = \frac{1}{\cos \theta} \sqrt{1 - \left(\frac{\sin \theta}{n} \right)^2} \quad (9.4.3)$$

$$\dots \sin x = \sqrt{1 - \cos^2 x} \quad (9.4.4)$$

$$F_x = \frac{1}{\cos \theta} \sqrt{1 - \left(\frac{\sqrt{1 - \cos^2 \theta}}{n} \right)^2} \quad (9.4.5)$$

$$F_x = \frac{1}{\cos \theta} \sqrt{1 - \frac{1 - \cos^2 \theta}{n^2}} \quad (9.4.6)$$

$$F_x = \frac{1}{\cos \theta} \sqrt{n^2 - 1 + \cos^2 \theta} \frac{1}{n} \quad (9.4.7)$$

$$F_x^2 = \frac{1}{\cos^2 \theta} (n^2 - 1 + \cos^2 \theta) \frac{1}{n^2} \quad (9.4.8)$$

$$F_x^2 n^2 = \frac{n^2}{\cos^2 \theta} - \frac{1}{\cos^2 \theta} + \frac{\cos^2 \theta}{\cos^2 \theta} \quad (9.4.9)$$

$$F_x^2 n^2 - 1 = \frac{n^2 - 1}{\cos^2 \theta} \quad (9.4.10)$$

$$\cos^2 \theta = \frac{n^2 - 1}{F_x^2 n^2 - 1} \quad (9.4.11)$$

$$\dots \cos^2 x = \frac{1 + \cos 2x}{2} \quad (9.4.12)$$

$$\cos 2\theta = 2 \left[\frac{n^2 - 1}{F_x^2 n^2 - 1} \right] - 1 \quad (9.4.13)$$

$$2\theta = \cos^{-1} \left(2 \left[\frac{n^2 - 1}{F_x^2 n^2 - 1} \right] - 1 \right) \quad (9.4.14)$$

9.5 Jones Matrices

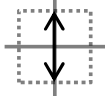
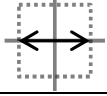
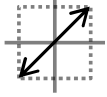
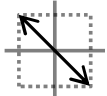
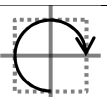
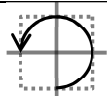
Polarization	Jones Vector	
Horizontal (x-axis)	$\begin{bmatrix} 1 \\ 0 \end{bmatrix}$	
Vertical (y-axis)	$\begin{bmatrix} 0 \\ 1 \end{bmatrix}$	
+45° from x-axis	$\frac{1}{\sqrt{2}} \begin{bmatrix} 1 \\ 1 \end{bmatrix}$	
-45° from x-axis	$\frac{1}{\sqrt{2}} \begin{bmatrix} 1 \\ -1 \end{bmatrix}$	
Right-hand Circular	$\frac{1}{\sqrt{2}} \begin{bmatrix} 1 \\ -i \end{bmatrix}$	
Left-hand Circular	$\frac{1}{\sqrt{2}} \begin{bmatrix} 1 \\ i \end{bmatrix}$	
Components		
Mirror	$\begin{bmatrix} 1 & 0 \\ 0 & -1 \end{bmatrix}$	
Quarter Waver Plate QWP	$\begin{bmatrix} 1 & 0 \\ 0 & \pm i \end{bmatrix}$	
Rotation element R(θ)	$\begin{bmatrix} \cos(\theta) & -\sin(\theta) \\ \sin(\theta) & \cos(\theta) \end{bmatrix}$	

Table 9.5.1: Jones matrices for various operations and components.

9.6 Fresnel Plots for Various Materials at 193 nm

